ARTICLES
https://doi.org/10.1038/s41590-021-01067-0
nature immunology

Check for updates

Homeostatic IL-13 in healthy skin directs dendritic cell differentiation to promote T_H2 and inhibit T_H17 cell polarization

Johannes U. Mayer[1,11], Kerry L. Hilligan[1,2], Jodie S. Chandler[1], David A. Eccles[1], Samuel I. Old[1], Rita G. Domingues[3], Jianping Yang[1], Greta R. Webb[1], Luis Munoz-Erazo[1], Evelyn J. Hyde[1], Kirsty A. Wakelin[1], Shiau-Choot Tang[1], Sally C. Chappell[1], Sventja von Daake[1], Frank Brombacher[4], Charles R. Mackay[5], Alan Sher[2], Roxane Tussiwand[6,7], Lisa M. Connor[1,12], David Gallego-Ortega[8,9], Dragana Jankovic[10], Graham Le Gros[1], Matthew R. Hepworth[3], Olivier Lamiable[1,13] and Franca Ronchese[1,13] ✉

The signals driving the adaptation of type 2 dendritic cells (DC2s) to diverse peripheral environments remain mostly undefined. We show that differentiation of CD11b^{lo} migratory DC2s—a DC2 population unique to the dermis—required IL-13 signaling dependent on the transcription factors STAT6 and KLF4, whereas DC2s in lung and small intestine were STAT6-independent. Similarly, human DC2s in skin expressed an IL-4 and IL-13 gene signature that was not found in blood, spleen and lung DCs. In mice, IL-13 was secreted homeostatically by dermal innate lymphoid cells and was independent of microbiota, TSLP or IL-33. In the absence of IL-13 signaling, dermal DC2s were stable in number but remained CD11b^{hi} and showed defective activation in response to allergens, with diminished ability to support the development of IL-4$^+$GATA3$^+$ helper T cells (T_H), whereas anti-fungal IL-17$^+$RORγt$^+$ T_H cells were increased. Therefore, homeostatic IL-13 fosters a noninflammatory skin environment that supports allergic sensitization.

Dendritic cells (DCs) have a crucial role in informing the adaptive immune system about infectious, innocuous and self antigens, and directing T cell responses towards effector activation or tolerance[1]. Two developmentally distinct lineages of DCs, termed 'type 1' (DC1) and 'type 2' (DC2) have been identified in all tissues in humans and mice[2]. DC1s are characterized by the expression of XCR1 and interact predominantly with CD8$^+$ T cells to cross-present cell-associated antigens and initiate immune responses against intracellular pathogens. By contrast, DC2s interact with CD4$^+$ T cells to promote T helper (T_H) and T regulatory cell (T_{reg}) cell responses[3].

DC2s from different tissues share several common characteristics that differentiate them from DC1s, including the expression of CD172a/Sirpα and being found in reduced numbers in the lymph nodes (LNs) of IRF4-deficient mice and humans[1,4]. Nonetheless, tissue DC2s are also heterogeneous in phenotype—a feature that is especially notable in the migratory DC2 population in nonlymphoid tissues[5,6]. Migratory DC2s from different tissues express unique markers that are largely conserved in mice and humans[2], suggesting that such heterogeneity is driven by the diverse requirements of each environment. While retinoic acid and TGF-β have been identified as factors necessary for the differentiation and functional maturation of intestinal CD103$^+$ DC2s (ref. [7]), it remains unclear whether and which tissue-derived signals guide DC2 differentiation at other sites.

The skin harbors four subsets of migratory DCs, each expressing a distinct transcriptomic signature[8]. The DC-like Langerhans cells (LC) are developmentally distinct from conventional DCs and are located in the epidermis. Dermal DCs include DC1 and DC2 populations, with the latter comprising CD11b^{hi} cells and a KLF4-dependent CD11b^{lo} subset that is necessary for induction of T_H2 responses[9].

As CD11b^{lo} DC2s are found only in skin[10], their differentiation may provide insight into the signals shaping the skin immune environment. We report that the development of CD11b^{lo} DC2s required the steady-state expression of interleukin 13 (IL-13) by

[1]Malaghan Institute of Medical Research, Wellington, New Zealand. [2]Immunobiology Section, Laboratory of Parasitic Diseases, National Institute of Allergy and Infectious Diseases, National Institutes of Health, Bethesda, MD, USA. [3]Lydia Becker Institute of Immunology and Inflammation, Manchester Collaborative Centre for Inflammation Research, Faculty of Biology, Medicine and Health, University of Manchester, Manchester Academic Health Science Centre, Manchester, UK. [4]International Centre for Genetic Engineering and Biotechnology (ICGEB), Cape Town component & Institute of Infectious Diseases and Molecular Medicine (IDM), Division of Immunology, Health Science Faculty, University of Cape Town, Cape Town, South Africa. [5]Infection and Immunity Program, Monash Biomedicine Discovery Institute, Monash University, Melbourne, VIC, Australia. [6]Department of Biomedicine, University of Basel, Basel, Switzerland. [7]Immune Regulation Unit, National Institute of Dental and Craniofacial Research, National Institutes of Health, Bethesda, MD, USA. [8]The Kinghorn Cancer Centre, Garvan Institute of Medical Research, Darlinghurst, NSW, Australia. [9]Centre for Single-Cell Technology, School of Biomedical Engineering, Faculty of Engineering and IT, University of Technology Sydney, Ultimo, NSW, Australia. [10]Immunoparasitology Unit, Laboratory of Parasitic Diseases, National Institute of Allergy and Infectious Diseases, National Institutes of Health, Bethesda, MD, USA. [11]Present address: Department of Dermatology and Allergology, Phillips University Marburg, Marburg, Germany. [12]Present address: School of Biological Sciences, Victoria University of Wellington, Wellington, New Zealand. [13]These authors contributed equally: Olivier Lamiable, Franca Ronchese. ✉e-mail: fronchese@malaghan.org.nz

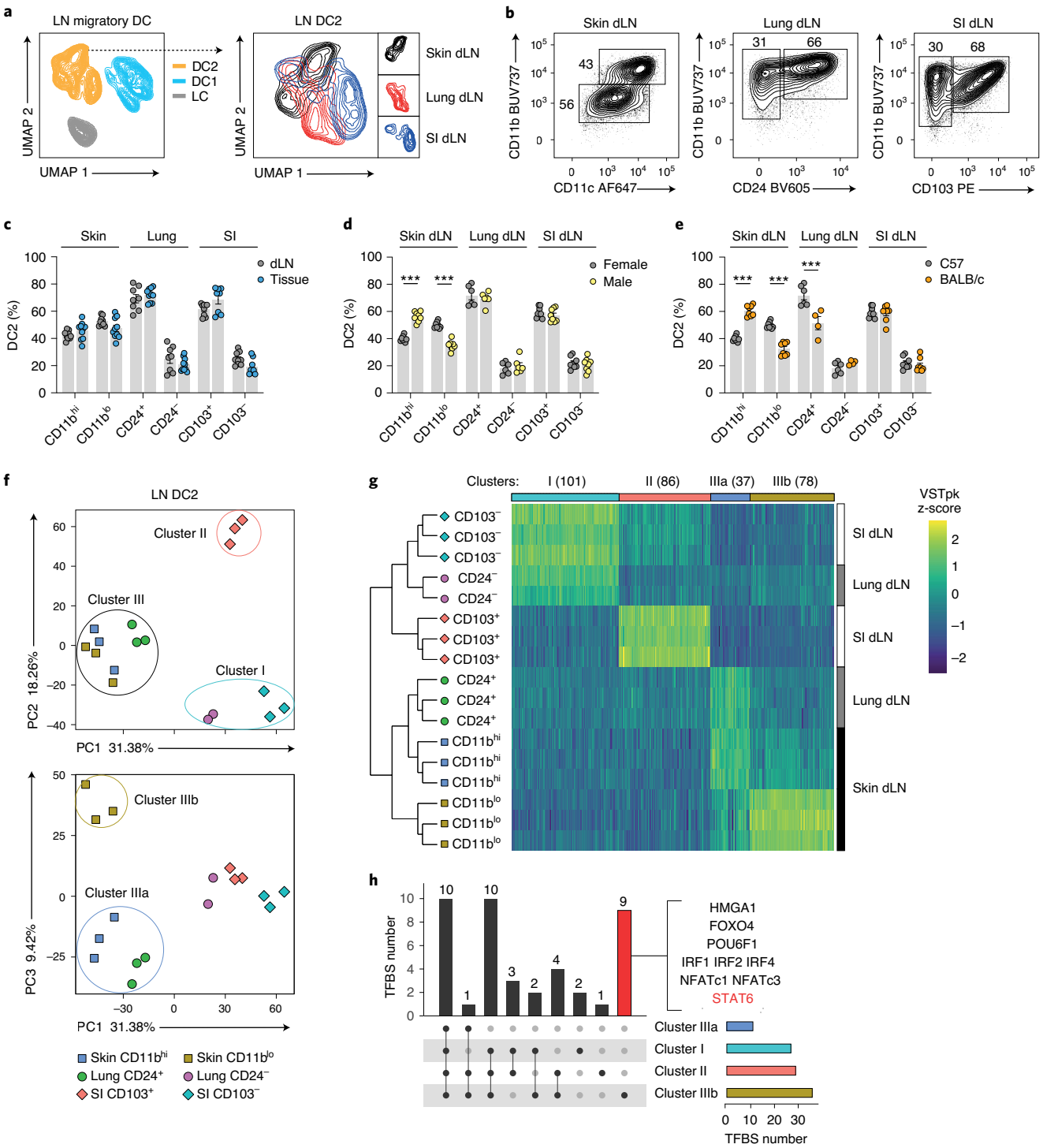

Fig. 1 | DC2s display tissue and subset-specific heterogeneity at steady state. a, Uniform manifold approximation and projection (UMAP) visualization of concatenated migratory DCs and DC2s from the skin, lung and SI dLN of naive C57BL/6 (C57) mice. DCs were gated as shown in Extended data Fig. 1. We performed UMAP on 150,000 events (10,000 events per tissue per mouse, 5 mice per group) using seven parameters (XCR1, CD326, Sirpα, CD11c, CD11b, CD24 and CD103) with default FlowJo settings of nearest neighbors =15 and minimum distance =0.5 using the Euclidean distance function. **b**, Phenotype of DC2 populations in the skin, lung and SI dLN of naive C57 mice. **c**, Relative frequencies of DC2 subsets within skin, lung and SI of naive C57 mice and their respective dLNs. **d**, Relative frequencies of DC2 subsets in the skin, lung and SI dLN of naive male and female C57 mice. **e**, Relative frequencies of DC2 subsets in the skin, lung and SI dLN of naive C57 and BALB/c mice. **f**, PC analysis of all expressed genes in DC2 subsets from the skin, lung and SI dLNs of naive C57 mice. **g**, Heatmap of differentially expressed genes for each of the clusters and subclusters in **f**. The number of genes in each cluster and subcluster is shown in parentheses at the top. z-scores for each gene were calculated using R. VSTpk, variance-stabilized transformed count per kilobase pair. **h**, UpSet plot showing the numbers of unique and shared TFBSs that were identified by TRANSFAC promoter analysis in each of the gene clusters in **g**. The number of TFBSs that are uniquely enriched in Cluster IIIb are indicated by the red bar with TFBSs listed on the right. **c**–**e**, Bar graphs show mean ± s.e.m. for $n = 8$–10 (**c**) $n = 6$–8 (**d**) and $n = 4$–8 (**e**) mice pooled from 2–3 (**c**) or 2 (**d**,**e**) independent experiments. Each symbol refers to one mouse. *P* values were determined using two-way ANOVA with Sidak's correction. ***$P < 0.001$; only significant comparisons are indicated.

ICOS$^+$KLRG1$^-$ST2$^-$ innate lymphoid cells (ILCs). Likewise, human DC2 populations from healthy skin, but not lung, expressed an IL-13 transcriptomic signature. Therefore, our data identify IL-13 as a skin 'niche factor' that drives steady-state DC2 differentiation and function.

Results

CD11b^{lo} skin DC2s express a STAT6-dependent signature. DC2s from the LNs draining (dLNs) the skin, lung and small intestine (SI) each express unique tissue-specific surface markers[2] and were defined as CD11b^{hi} and CD11b^{lo} in the skin dLN, CD24$^+$ and CD24$^-$ in the lung dLN, and CD103$^+$ and CD103$^-$ in the SI dLN (Fig. 1a,b and Extended data Fig. 1a). These same phenotypes were observed also in the respective tissues (Fig. 1c and Extended data Fig. 1b), in males and females (Fig. 1d) and BALB/c and C57BL/6 (C57) mice (Fig. 1e), indicating that these DC2 subsets are conserved across different mice and strains. All DC2 subsets were significantly reduced in number in the dLN of *Irf4*$^{f/f}$ CD11c-Cre compared with *Irf4*$^{f/f}$ mice (Extended data Fig. 1c), confirming that they represented bona fide DC2s (ref. [2]).

A principal component (PC) analysis (PCA) of all expressed genes in migratory DC2s from the skin, lung and SI dLN of naive C57 mice revealed three main clusters on PC1 versus PC2 (Fig. 1f). Cluster I included CD103$^-$ and CD24$^-$ DC2s from the SI and lung dLN, respectively; SI dLN CD103$^+$ DC2 formed cluster II, and cluster III included both skin dLN DC2 subsets and CD24$^+$ DC2 from the lung dLN. PC3 further resolved cluster III into skin dLN CD11b^{hi} and lung dLN CD24$^+$ DC2s, forming cluster IIIa, and skin dLN CD11b^{lo} DC2s in cluster IIIb. Each cluster expressed a specific transcriptional signature that included a variable number of genes (Fig. 1g and Supplementary Table 1).

Analysis of the promoter sequences of cluster-specific genes for enriched transcription factor binding sites (TFBSs) revealed that most TFBSs were shared across multiple clusters (Fig. 1h and Supplementary Table 2). Amongst the nine TFBS specifically enriched in cluster IIIb was STAT6, a transcription factor with no described role in DC2 biology at steady state. As STAT6 is essential for signaling by the T_H2 cytokines IL-4 and IL-13 (ref. [11]), the enrichment of STAT6-binding sites only in CD11b^{lo} DC2 signature genes suggested that these DCs had been exposed to IL-4 and/or IL-13 in vivo.

Differentiation of CD11b^{lo} DC2s requires STAT6 signaling. To determine whether STAT6 signaling has a role in DC2 development, we identified the Lin$^-$CD11c$^+$MHCII$^-$CD135$^+$ preDC populations in the bone marrow (BM) and ear skin of C57 and STAT6-deficient (hereafter STAT6 KO) mice (Extended data Fig. 2a). BM and skin preDC2s (ref. [12]) were present in both mouse strains in similar frequencies (Fig. 2a), indicating a comparable development and egress from the BM, and were similarly CD11b^{hi} in skin (Fig. 2a), suggesting that downregulation of CD11b in dermal CD11b^{lo} DC2s occurs during maturation in the skin.

Analysis of mature DC subsets revealed that the frequencies of CD11b^{lo} DC2s in ear skin and dLN were significantly reduced in STAT6 KO mice compared with C57, whereas skin CD11b^{hi} DC2s were correspondingly increased and DC2 subsets in lung and SI were unchanged (Fig. 2b–e). The frequencies of DC1s and LCs in skin and skin dLN (Fig. 2c,e) and myeloid populations in skin (Extended data Fig. 2b) were also similar in both mouse strains. Comparable variations were observed in the numbers of migratory DCs in the ear skin, lung and SI dLN of STAT6 KO and C57 mice (Extended data Fig. 2c,d), and DC2 subsets in LNs draining other areas of the skin including forelimb, hindlimb and trunk (Extended data Fig. 2e) indicating that CD11b^{lo} DC2s undergo a similar developmental program irrespective of skin region.

To further explore the impact of STAT6 signaling on DC2s, we compared global gene expression in DC2 subsets from the skin, lung and SI dLNs of C57 and STAT6 KO mice (Supplementary Table 3). A PCA comparing skin dLN DC2s from C57 and STAT6 KO mice showed that CD11b^{hi} and CD11b^{lo} DC2 subsets split across PC1 (Extended data Fig. 2f,g), suggesting that both subsets maintained their transcriptional identity. However, C57 and STAT6 KO CD11b^{hi} and CD11b^{lo} DC2s clustered separately along PC2 and PC3, respectively, suggesting that STAT6 controls the expression of multiple genes in both populations. PCAs comparing lung and SI dLN DC2s showed that C57 and STAT6 KO DC2s clustered together on both PC1 and PC2, confirming the overall similarity of each population across genotypes (Extended data Fig. 2f).

To better understand the heterogeneity of CD11b^{hi} and CD11b^{lo} DC2s in C57 and STAT6 KO mice, we performed single-cell RNA sequencing (scRNA-seq) on sorted skin dLN SIRPα$^+$ DC2s. The 983 C57 and 1,120 STAT6 KO cells that passed quality control (QC) were analyzed by dimensionality reduction and clustering. We identified three clusters (Fig. 2f), of which two expressed high levels of CD11b^{hi} signature transcripts with low CD11b^{lo} transcripts (Fig. 2g); we named these clusters CD11b^{hi} DC2-1 and DC2-2. CD11b^{hi} DC2-1 highly expressed *Ccl5* and *Cd44*, while CD11b^{hi} DC2-2 were enriched for the proinflammatory cytokine *Il1b* and the antiapoptotic genes *Bcl2a1b* and *Bcl2a1d* (Supplementary Table 4) suggesting that DC2-1 and DC2-2 were distinguished by their maturation and survival status. The third cluster preferentially expressed transcripts specific for CD11b^{lo} DC2s and low CD11b^{hi} transcripts (Fig. 2f,g), identifying this cluster as CD11b^{lo} DC2s. This cluster was underrepresented in STAT6 KO compared with C57, whereas the CD11b^{hi} DC2-1 and DC2-2 clusters were overrepresented (Fig. 2h), reproducing our flow cytometry data. Fewer than 15 genes were expressed differentially in STAT6 KO compared with C57 DC2s in each of the three clusters (Supplementary Table 4), indicating that STAT6 controls the differentiation of CD11b^{lo} DC2s without affecting the transcriptional phenotype of CD11b^{hi} DC2s. These data suggest that STAT6 signaling is required for the differentiation of CD11b^{lo} DC2s in all areas of skin and their dLNs, whereas CD11b^{hi} DC2s and DC2 subsets in lung and intestine are STAT6-independent.

IL-13 is necessary for CD11b^{lo} DC2 differentiation. To establish whether STAT6 signaling was intrinsically required for CD11b^{lo} DC2 development, we generated mixed wild type and STAT6 KO

Fig. 2 | STAT6-dependent signaling controls CD11b^{lo} DC2 differentiation at steady state. a, Phenotype and frequency of DC2 precursors in the BM and skin of naive C57 and STAT6 knockout (KO) mice, as gated in Extended data Fig. 2a. Data are concatenated from four to five mice. PreDC2 are identified by the gates and quantified in the bar graphs. Histograms on the right show CD11b expression on skin DC2 precursors and fluorescence-minus-one (FMO) controls. **b**, Phenotype of DC2 populations in the skin, lung and SI of naive C57 and STAT6 KO mice. **c**, Relative frequencies of DC2 (left) and DC (right) subsets in the skin, lung and SI of naive C57 and STAT6 KO mice. **d**, Phenotype of DC2 populations in the skin, lung and SI dLNs of naive C57 and STAT6 KO mice. **e**, Relative frequencies of migratory DC2 (left) and DC (right) subsets in the skin, lung and SI dLN of naive C57 and STAT6 KO mice. **f**, UMAP visualization of scRNA-seq data from migratory DC2s in the skin dLNs of C57 or STAT6 KO mice. **g**, Heatmap and dotplot showing the expression of selected markers that discriminate between CD11b^{hi} and CD11b^{lo} DC2 subsets in skin dLN. Bulk RNA-seq (left) and scRNA-seq (right) data are shown. **h**, Bar graphs showing the numbers (left) and percentages (right) of C57 and STAT6 KO DC2s in each cluster. **a**,**c**,**e**, Bar graphs show mean ± s.e.m. for $n = 6$ (**a**, BM), $n = 9$–10 (**a**, skin), $n = 7$–11 (**c**), $n = 4$–5 (**e**, left) or $n = 9$–10 (**e**, right) mice pooled from two (**a**,**e**) or two to three (**c**) independent experiments. Each symbol refers to one mouse. *P* values were determined using two-way ANOVA with Sidak's correction. ***$P < 0.001$; only significant comparisons are indicated.

BM chimeras in wild-type hosts. Wild-type DC2s in skin and skin dLNs developed into CD11b^{hi} and CD11b^{lo} populations, whereas STAT6 KO-derived DC2s remained mostly CD11b^{hi} (Fig. 3a and Extended data Fig. 3a). Because the activation of STAT6 is mediated by the cytokines IL-4 and IL-13 through the type I IL-4 receptor or the type II IL-4 and IL-13 receptor[11], we assessed dermal DC2s in mice lacking these cytokines or their receptors. Naive IL-4 KO mice had a normal distribution of CD11b^{hi} and CD11b^{lo} DC2s in the skin and dLN, whereas IL-13 KO, IL-4Rα KO and IL-13Rα1 KO mice showed a reduction in CD11b^{lo} DC2s comparable with that observed in STAT6 KO mice (Fig. 3b,c and Extended Data Fig. 3b–d). Transcripts for *Il2rg*, *Il4ra*, *Il13ra1* and other members of the IL-13 signaling pathway[11] (Fig. 3d) as well as the IL-4Rα and IL-13Rα1 proteins (Fig. 3e) were expressed at similar levels by all DC2 subsets from lung, SI and skin dLN, suggesting a similar capacity to respond to IL-13. Consistent with the predicted role of

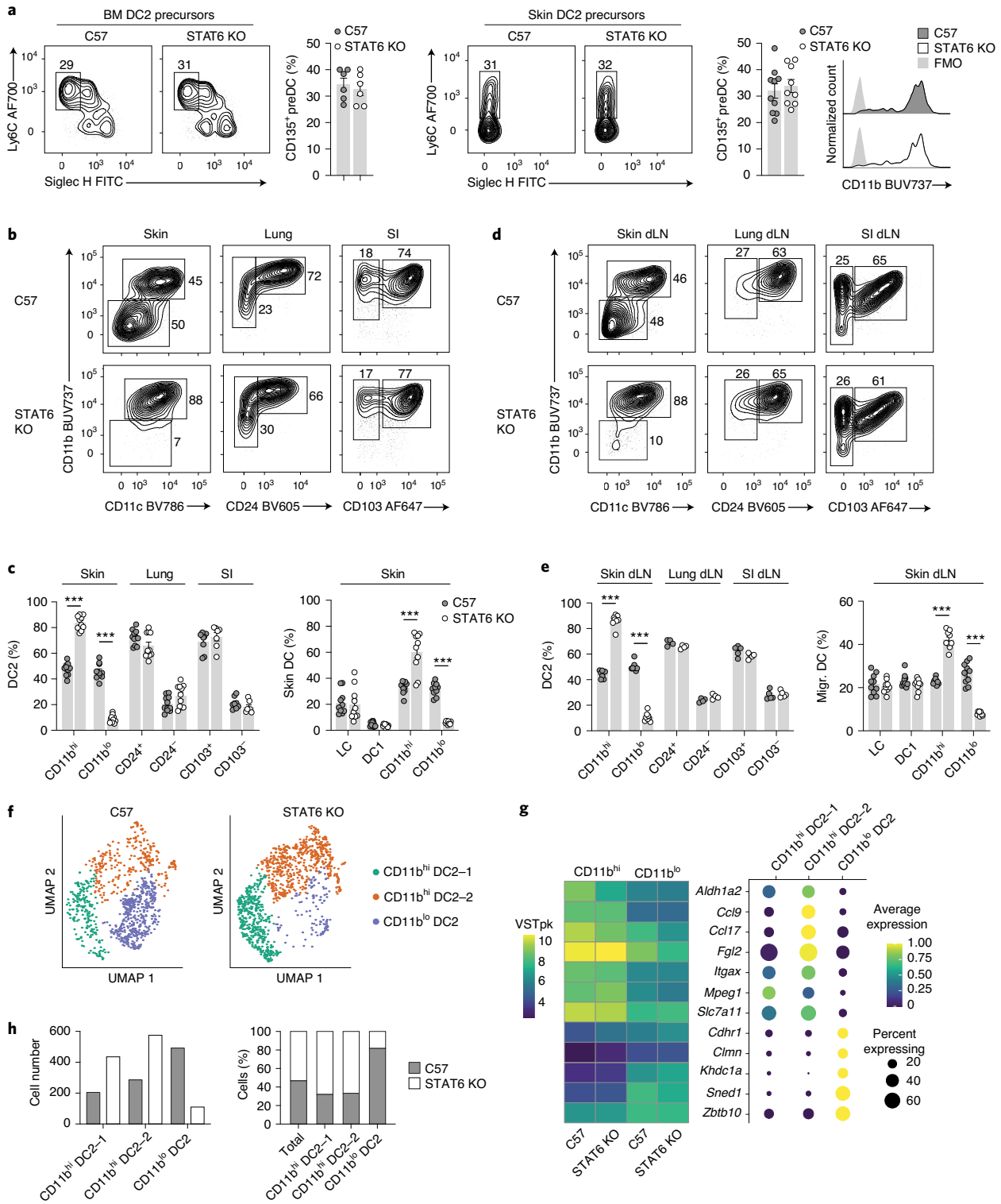

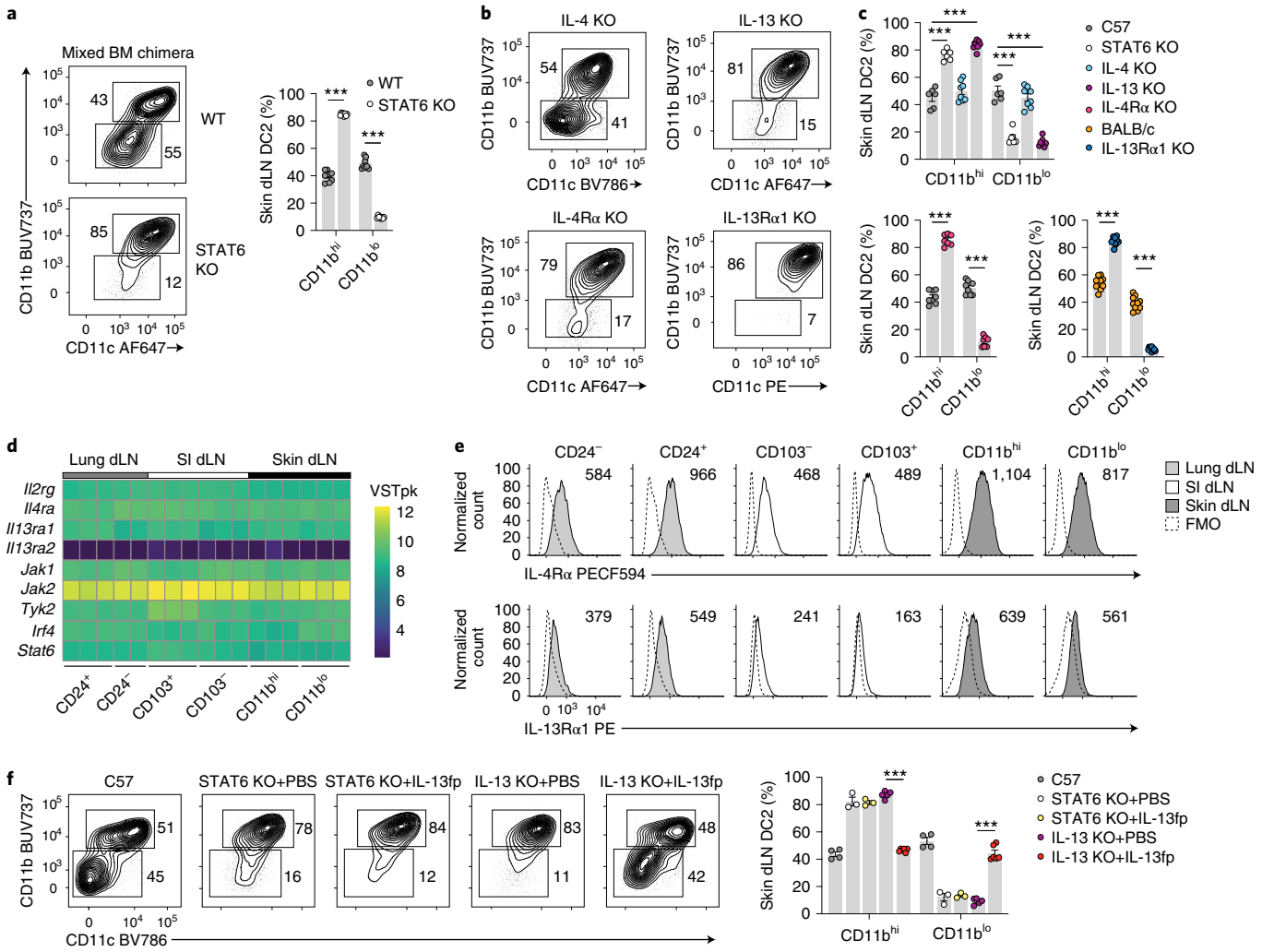

Fig. 3 | IL-13 is necessary for the differentiation of dermal CD11b^{lo} DC2s in vivo. a, Phenotype of skin dLN DC2s in (wild-type (WT) + STAT6 knockout (KO))→WT mixed BM chimeras; each donor BM is shown separately. DC2 subsets are quantified in the bar graph. **b**, Phenotype of skin dLN DC2s in naive mice of the strains indicated. All KO strains were on a C57BL/6 (C57) background except for the IL-13Rα1 KO which was on a BALB/c background. **c**, Relative frequencies of skin dLN DC2 subsets in naive mice of the indicated strains. **d**, Heatmap showing expression of transcripts associated with the IL-4 and IL-13 signaling pathway in DC2 subsets from the lung, skin and SI dLNs of naive C57 mice. Each column refers to one biological replicate. VSTpk, variance-stabilized and transformed read counts per kilobase pair. **e**, IL-4Rα and IL-13Rα1 expression on DC2 subsets from the lung, skin and SI dLNs of C57 mice. Histograms show concatenated data from four mice in one of two independent experiments that gave similar results. **f**, Phenotype of skin dLN DC2s in C57 controls and mutant mice that were treated i.p. with either PBS or IL-13fp for 4 days before analysis. DC2 subsets are quantified in the bar graph. **a**,**c**,**f**, Bar graphs show mean ± s.e.m. for $n = 8$ chimeras (**a**) or $n = 6$–10 (**c**) or $n = 3$–6 (**f**) mice pooled from two (**a**,**c**, IL-13 KO in **f**) or one (C57 and STAT6 KO in **f**) independent experiments. Each symbol refers to one chimera or one mouse. *P* values were determined using two-way ANOVA with Sidak's (**a**,**c**) or Tukey's (**f**, for IL-13 KO only) correction. ***$P < 0.001$; only relevant significant comparisons are indicated.

IL-13, treatment of STAT6 KO and IL-13 KO mice with recombinant IL-13 (rIL-13) fusion protein (IL-13 fp) rescued the development of CD11b^{lo} skin DC2s in IL-13 KO mice to frequencies similar to those in C57 controls (Fig. 3f) without affecting DC2s in STAT6 KO mice or the expression of CD11b, CD24 and CD103 on DC2s in lung and SI dLN (Extended data Fig. 3e,f). Therefore, direct IL-13 signaling is essential for the differentiation of skin CD11b^{lo} DC2s but is not sufficient to drive the development of CD11b^{lo} DC2 in lung or SI.

ICOS$^+$ ILCs are the predominant source of IL-13 in skin. To identify the source of IL-13 in skin, we used 4C13R mice[13], which report *Il13* expression through DsRed (DR) (Extended data Fig. 4a). *Il13*-DR was highly expressed by about 30% of skin ILCs, while other innate and adaptive immune cells expressed *Il13*-DR at low intensity and at frequencies below 5% (Fig. 4a). Lin$^-$CD90$^+$CD127$^+$ ILCs were the most abundant *Il13*-DR$^+$ skin cell population, followed by the TCRγδ^{hi} dendritic epidermal T cells (DETCs) (Fig. 4b). At steady state, *Il13*-DR$^+$ ILCs were identified in the skin, but not in the lung or SI of 4C13R mice (Fig. 4c), and their proportion was higher in females compared with males (Fig. 4d). RAG1 KO mice, which lack all adaptive and innate-like T cells showed no impairment in the differentiation of CD11b^{lo} DC2s in the skin and skin dLN (Fig. 4e), confirming ILCs as the likely source of IL-13 in skin.

Il13-DR$^+$ and *Il13*-DR$^-$ skin ILCs were *Il4*-AmCyan^{lo}CD44^{hi}ICOS$^+$ (Fig. 4f and Extended data Fig. 4b). However, unlike lung ILCs acquired using the same isolation protocol, skin ILCs were ST2^{lo}CD25^{lo}KLRG1^{lo} (Fig. 4f), which is consistent with the described phenotype of dermal ILCs[14,15]. About 50% of skin ILCs expressed the transcription factor GATA3, while fewer than 10% expressed

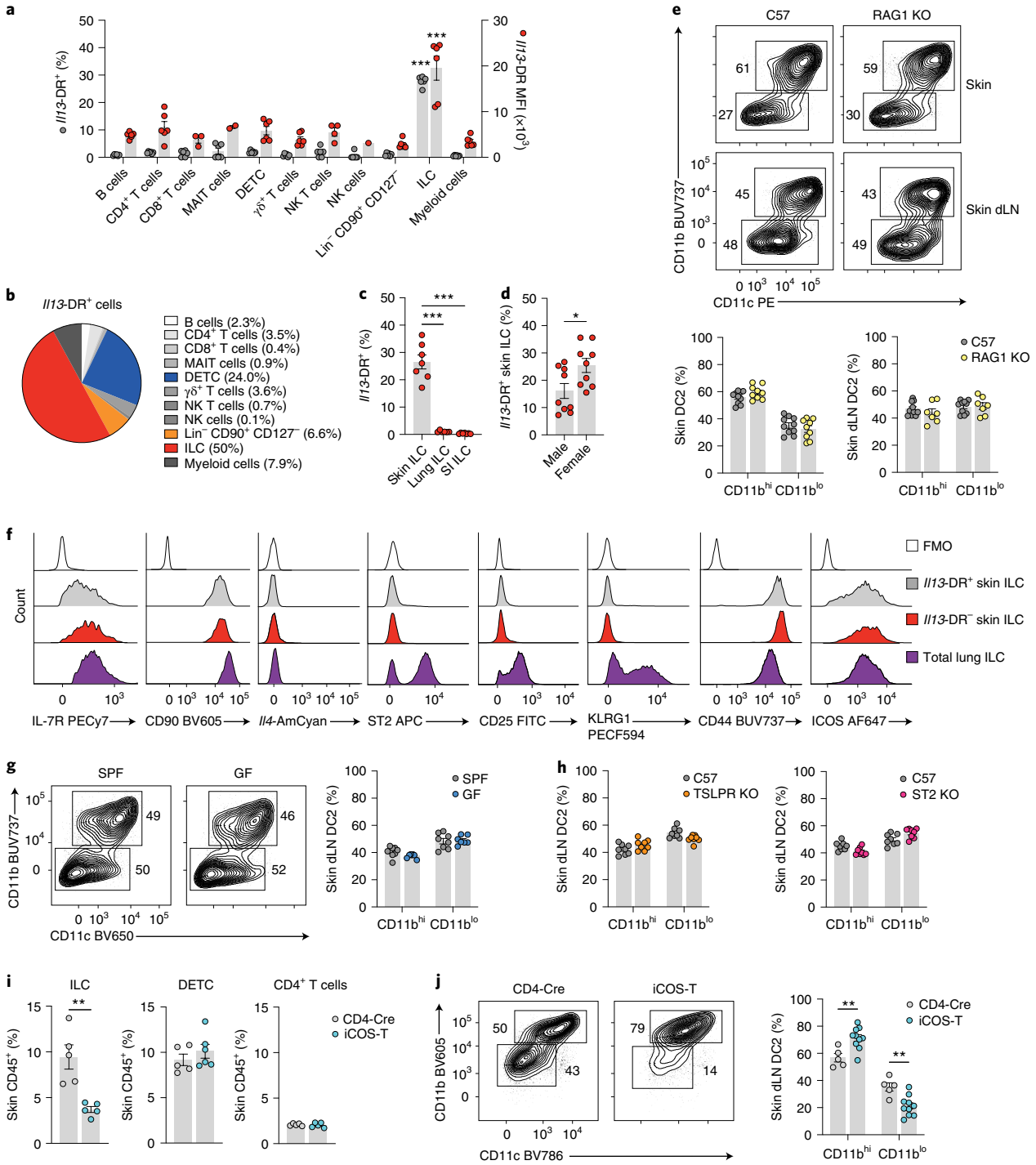

Fig. 4 | Homeostatic IL-13 is produced by skin innate lymphoid cells irrespective of microbial or alarmin signaling and promotes the differentiation of CD11b^{lo} DC2s. a, Frequencies of *Il13*-DR$^+$ cells and *Il13*-DR median fluorescence intensities (MFI) within different populations of innate and adaptive immune cells in the ear skin of naive 4C13R reporter mice. *P* values refer to the comparison of ILCs with each of the other populations. **b**, Pie chart showing the proportions of different immune cell populations within the total *Il13*-DR$^+$ population. Data are from **a**. **c**, Frequencies of *Il13*-DR$^+$ ILCs in the skin, lung and SI of naive 4C13R mice. **d**, Frequencies of *Il13*-DR$^+$ ILCs in the skin of male and female naive 4C13R reporter mice. **e**, Phenotype of skin and skin dLN DC2s in naive C57BL/6 (C57) and RAG1 KO mice. Relative subset frequencies are quantified in the bar graphs. **f**, Phenotype of *Il13*-DR$^-$ and *Il13*-DR$^+$ ILCs from skin, and total ILCs from lung of naive 4C13R reporter mice. Histograms show concatenated data from four mice in one of four independent experiments that gave similar results. **g**, Phenotype of skin dLN DC2s in specific pathogen-free (SPF) or germ-free (GF) naive C57 mice. Relative subset frequencies are quantified in the bar graph. **h**, Relative frequencies of skin dLN DC2 subsets in naive TSLPR KO, ST2 KO and C57 control mice. **i**, Frequencies of ILC, DETC and CD4$^+$ T cell populations in the skin of male CD4-Cre and iCOS-T mice treated with DT. **j**, Phenotype of skin dLN DC2 subsets in male CD4-Cre and iCOS-T mice treated with DT. DC2 subsets are quantified in the bar graph. **a–j**, Bar graphs shows mean ± s.e.m. for $n = 6$ samples of three pooled mice each (**a**) or $n = 6$–7 (**c**), $n = 9$ (**d**), $n = 8$–10 (**e**), $n = 7$–8 (**g**), $n = 8$ (**h**), $n = 5$ (**i**) or $n = 5$–10 (**j**) mice pooled from two (**a**,**c**–**e**,**g**,**h**,**j**) independent experiments, or from one of two repeat experiments that gave similar results (**i**). Each symbol refers to one sample or one mouse. *P* values were determined using one-way (**a**,**c**) or two-way (**e**,**g**,**h**,**j**) ANOVA with Sidak's correction, or a two-tailed Student's *t*-test (**d**,**i**). $^*P < 0.05$; $^{**}P < 0.01$; $^{***}P < 0.001$; only significant comparisons are indicated.

T-bet or RORγt (Extended data Fig. 4c). Germ-free (GF), TSLPR KO and ST2 KO mice had normal numbers of CD11b^{lo} DC2s (Fig. 4g, h), indicating that microbiota and skin alarmins were not essential for steady-state IL-13 production in skin.

Diphtheria toxin (DT) treatment of *Icos*-DTR$^{fl/+}$ CD4-Cre (iCOS-T[16]) mice enables the depletion of ICOS$^+$ ILCs while preserving ICOS$^+$ CD4$^+$ T cells due to the Cre-dependent deletion of the DTR gene only in CD4$^+$ T cells[16]. DT treatment for 9 days led to a greater than 50% reduction in total skin ILCs with no impact on TCRγδ^{hi} DETCs or CD3$^+$CD4$^+$ T cells (Fig. 4i), and an approximately 50% decrease in the frequency of CD11b^{lo} DC2s in iCOS-T mice compared with CD4-Cre controls (Fig. 4j). Thus, dermal ICOS$^+$ ILCs are the main source of IL-13 for the differentiation of CD11b^{lo} DC2s at steady state.

IL-13 signaling requires KLF4 expression in DCs. To model the differentiation of CD11b^{lo} DC2s in vitro, we treated FLT3L BM DCs (BMDCs)[17] with rIL-13. Treatment with rIL-13 induced the differentiation of a population of CD11b^{lo} BMDC2s (Extended data Fig. 5a–c), which were IL-4Rα and STAT6-dependent (Fig. 5a), and downregulated several genes highly expressed in CD11b^{hi} DC2s from skin dLN while upregulating transcripts highly expressed in CD11b^{lo} DC2s in vivo (Fig. 5b). Supplementation of *Klf4*$^{f/f}$ BMDC cultures with rIL-13 resulted in similar frequencies of CD11b^{lo} BMDCs as the CD11b^{lo} cells in C57 BMDC cultures, whereas *Klf4*$^{f/f}$ Vav-iCre BMDC cultures remained CD11b^{hi} (Fig. 5c). Similarly, in vivo treatment of *Klf4*$^{f/f}$ Vav-iCre→C57 chimeric mice with IL-13fp did not rescue the differentiation of CD11b^{lo} DC2s to the level observed in *Klf4*$^{f/f}$→C57 control chimeras (Fig. 5d), despite similar expression of IL-4Rα and IL-13Rα1 in *Klf4*$^{f/f}$ and *Klf4*$^{f/f}$ Vav-iCre CD11b^{hi} DC2s (Extended data Fig. 5d).

As assessed by phosphoimmunofluorescence, pY641 STAT6 was readily detectable in the nuclear area of C57, *Klf4*$^{f/f}$ and *Klf4*$^{f/f}$ Vav-iCre Sirpα$^+$ BMDCs exposed to rIL-13 (Fig. 5e), but was not detected in IL-4Rα KO, STAT6 KO or untreated BMDC cultures (Extended Data Fig. 5e), indicating that the phosphorylation of STAT6 is functional in KLF4 KO DC and is presumably upstream of KLF4. Thus KLF4 controls DC2 responsiveness to IL-13 in vitro and in vivo.

IL-13 signaling in DC2s regulates T_H cell polarization. To investigate the impact of IL-13 signaling on DC2 function, we generated mixed BM chimeric mice in which STAT6-competent CD45.1/CD45.2 CD4$^+$ T cells were derived from MHCII KO BMs, whereas MHCII-competent CD45.2 DCs were either responsive to IL-13 in the control C57 chimeras, or unable to respond in the STAT6 KO chimeras (Extended Data Fig. 6a–d). All chimeras were immunized intradermally with inactivated *Mycobacterium smegmatis* (*Ms*), *Nippostrongylus brasiliensis* L3 larvae (*Nb*) or *Candida albicans* (*Ca*) to induce T_H1, T_H2 or T_H17 responses[18,19]. IFN-γ$^+$ T_H cells induced by *Ms* were detected in similar numbers in the C57 and STAT6 KO mixed BM chimeras (Fig. 6a), while the numbers of IL-4$^+$ and IL-13$^+$ T_H cells induced by *Nb* were significantly reduced, and the numbers of IL-17A$^+$ T_H cells induced by *Ca* trended towards an increase in the STAT6 KO compared with C57 mixed BM chimeras (Fig. 6a). Similar variations were observed in the frequencies of CD44^{hi} cells in the CD4$^+$ T cell population (Fig. 6b), suggesting that IL-13 signaling in DCs is important for the induction of T_H2 cells and may be limiting the differentiation of T_H17 cells.

In a separate model, we generated *Il4ra*$^{f/-}$ zDC-Cre mice, in which conditional deletion of the IL-4 and IL-13 receptors in DCs results in impaired development of CD11b^{lo} DC2s (Extended Data Fig. 6e). Immunization with *Ms* generated similar numbers of IFN-γ$^+$ CD4$^+$ T cells in *Il4ra*$^{f/-}$ zDC-Cre and *Il4ra*$^{f/-}$ mice, whereas the numbers of IL-4$^+$, IL-13$^+$ and GATA3$^+$ T_H cells after *Nb* immunization were reduced, and the numbers of IL-17A$^+$ and RORγt$^+$ T_H cells after *Ca* were increased in *Il4ra*$^{f/-}$ zDC-Cre compared with *Il4ra*$^{f/-}$ mice (Fig. 6c,d and Extended Data Fig. 6f). The numbers and frequencies of activated CD44^{hi}CD4$^+$ T cells in *Il4ra*$^{f/-}$ zDC-Cre and *Il4ra*$^{f/-}$ mice (Fig. 6e and Extended Data Fig. 6g) reproduced the differences observed in the numbers of cytokine-expressing T cells after immunization (Fig. 6c). In addition, the numbers of GATA3$^+$ cells in spleen were significantly lower in *Il4ra*$^{f/-}$ zDC-Cre mice compared with *Il4ra*$^{f/-}$(Fig. 6f), indicating that the systemic T_H2 response was also impaired. The frequencies of FoxP3$^+$CD25$^+$CD4$^+$ T cells in naive and *Nb* or *Ca*-immunized mice were similar between *Il4ra*$^{f/-}$ zDC-Cre and *Il4ra*$^{f/-}$ mice, with similar levels of FoxP3 expression and a comparable upregulation after immunization (Fig. 6g), suggesting similar Treg cell activation regardless of *Il4ra* expression in DCs.

To assess whether the impact of IL-4Rα expression on DC function was specific to skin, we compared T_H2 responses after immunization with house dust mite (HDM) extract given either intradermally or intranasally (i.n.). Intradermal HDM immunization increased the number of GATA3$^+$CD4$^+$ T cells in dLN, and this increase was greater in *Il4ra*$^{f/-}$ compared with *Il4ra*$^{f/-}$ zDC-Cre mice (Fig. 6h). In contrast, i.n. HDM immunization increased the number of GATA3$^+$CD4$^+$ T cells in the mediastinal LN to a similar extent in *Il4ra*$^{f/-}$ zDC-Cre and *Il4ra*$^{f/-}$ mice (Fig. 6h). Thus, steady-state IL-13 signaling in dermal DC2s specifically enhances T_H2 responses after intradermal immunization.

Antigen uptake by dermal DC2 was assessed by injection of fluorescently labeled *Nb* (*Nb*-AF488). The total number of *Nb*-AF488$^+$ cells in skin dLN was around 20% lower in *Il4ra*$^{f/-}$ zDC-Cre mice compared with *Il4ra*$^{f/-}$ (Fig. 7a and Extended Data Fig. 6h). Moreover, most AF488$^+$ cells in *Il4ra*$^{f/-}$ mice were CD11b^{lo} DC2s followed by CD11b^{hi} DC2s, whereas AF488$^+$ cells in *Il4ra*$^{f/-}$ zDC-Cre mice were predominantly CD11b^{hi} DC2s and monocytes (Fig. 7b,c and Extended Data Fig. 6i,j). Because the DC signals that drive the development of T_H2 responses are not defined[20], we examined the expression of several activation markers on DCs[21–24]. AF488$^+$CD11b^{hi} DC2s expressed similar activation marker profiles in *Il4ra*$^{f/-}$ and *Il4ra*$^{f/-}$ zDC-Cre mice, with high levels of the costimulatory molecules CD86 and PDL2 and the interferon response genes BST2 and Ly6A/E (Fig. 7d). Compared with CD11b^{hi} DC2, the AF488$^+$CD11b^{lo} DC2s in *Il4ra*$^{f/-}$ mice expressed higher CD86 and PDL2 and lower Bst2 and Ly6A/E[22], whereas the few AF488$^+$ CD11b^{lo} DC2s in *Il4ra*$^{f/-}$ zDC-Cre mice expressed a profile more similar to CD11b^{hi} than to CD11b^{lo} DC2s in the *Il4ra*$^{f/-}$ mice (Fig. 7d). Thus lack of IL-13 signaling results in lower expression of CD86 and PDL2 on *Nb*-AF488$^+$ DC2s in dLN.

To investigate the increased responses to *Ca* in *Il4ra*$^{f/-}$ zDC-Cre mice, we assessed expression of innate pattern recognition receptors in DC2 subsets[25]. Expression of *Clec7a* and *Clec4n*, encoding dectin-1 and dectin-2, respectively, and *Tlr1*, *Tlr2*, *Tlr6*, *Tlr11* and the TLR chaperone *Unc93b1*, was significantly higher in CD11b^{hi} compared with CD11b^{lo} DC2s (Fig. 7e). CD11b^{hi} DC2s, but not CD11b^{lo} DC2s upregulated expression of *Il23a* and *Il12b* transcripts after *Ca* immunization, and highly expressed the α4β8 integrin subunit *Itgb8* (Fig. 7e), which is necessary for the conversion of latent TGFβ to the active form during T_H17 differentiation[26,27]. Both DC2 subsets upregulated *Il6*, while *Il1b* was expressed but not upregulated after *Ca* uptake (Fig. 7e). In *Il12b*-YFP reporter mice immunized with *Ca* labeled with cell tracker orange CMTMR (*Ca*-CTO), only CD11b^{hi} *Ca*-CTO$^+$ DC2s were *Il12b*-YFP^{hi} (Fig. 7f,g). Therefore, a higher frequency of CD11b^{hi} DC2s in *Il4ra*$^{f/-}$ zDC-Cre mice could favor the observed increase in IL-17A responses in these mice.

Human skin DC2s express an IL-4/IL-13 signature. To assess IL-13 signaling in human skin, we selected four published transcriptomic datasets that compared tissue DC2s from the skin or lung of healthy individuals with DC2s from blood or spleen (Fig. 8a).

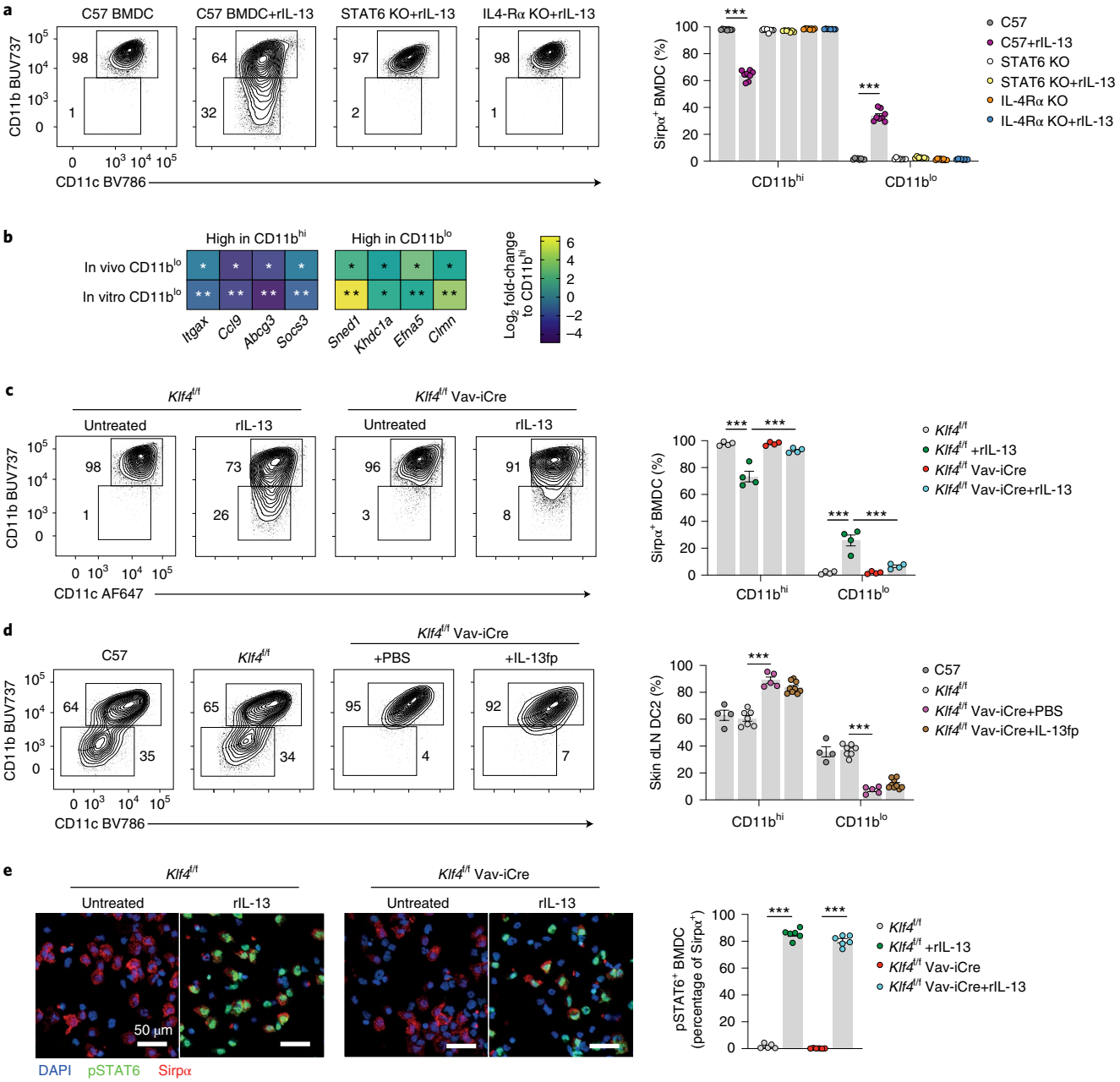

Fig. 5 | IL-13 signaling drives the development of CD11b^{lo} DC2s in vitro and requires KLF4 expression in DCs. a, Phenotype of Sirpα$^+$ cells in FLT3L BMDC cultures from mice of the indicated mouse strains. C57BL/6 (C57) cultures were untreated or supplemented with rIL-13. Relative subset frequencies are quantified in the bar graph. **b**, Heatmaps showing mean relative expression of CD11b^{hi} and CD11b^{lo} DC2 signature transcripts in sorted DC2 subpopulations from C57 skin dLN (in vivo) or C57 FLT3L BMDC cultures that were untreated or treated with rIL-13 (in vitro). Transcript levels were measured by RT-qPCR. Values refer to $n=8$ independently treated cultures (in vitro) or $n=6$ mice (in vivo) pooled from two independent experiments. *P* values were determined using a paired, two-tailed Wilcoxon *t*-test comparing the relative expression of CD11b^{hi} and CD11b^{lo} DC2 transcripts. $^*P<0.05$; $^{**}P<0.01$. **c**, Phenotype of Sirpα$^+$ FLT3L BMDCs from *Klf4*$^{f/f}$→C57 or *Klf4*$^{f/f}$ Vav-iCre→C57 male chimeric donors. Cultures were untreated or supplemented with rIL-13. Relative subset frequencies are quantified in the bar graph. **d**, Phenotype of DC2 subsets in the skin dLNs of C57 or chimeric *Klf4*$^{f/f}$→C57 or *Klf4*$^{f/f}$ Vav-iCre→C57 mice. Mice were treated with PBS or IL-13fp as indicated. Relative subset frequencies are quantified in the bar graph. **e**, Representative images of FLT3L BMDC cultures from *Klf4*$^{f/f}$→C57 or *Klf4*$^{f/f}$ Vav-iCre→C57 male chimeric donors. Cultures were either unstimulated or treated with 100 ng ml^{-1} rIL-13 for 30 min before staining. Scale bars, 50 μm. pSTAT6$^+$ cells in the Sirpα$^+$ population are quantified in the bar graph. An average of 2,200 Sirpα$^+$ cells per sample were assessed. Data from control cultures are shown in Extended Data Fig. 5e. **a**,**c**,**d**,**e**, Bar graphs show mean ± s.e.m. for $n=7$–8 (**a**), $n=4$ (**c**), or $n=5$–6 (**e**) independently treated culture wells, or $n=4$–9 (**d**) mice pooled from two (**a**,**d**,**e**) or three (**c**) independent experiments. Each symbol refers to one culture or one mouse. *P* values were determined using two-way (**a**,**c**,**d**) or one-way (**e**) ANOVA with Tukey's correction. $^{***}P<0.001$; only relevant significant comparisons are indicated.

We examined each set of DEGs using gene set enrichment analysis (GSEA)[28] and the Reactome database[29]. We found that most enriched pathways were unique to one or a few individual comparisons (Fig. 8a and Supplementary Table 5). The 'IL-4 and IL-13 signaling' pathway was one of the four pathways that were significantly enriched in all comparisons of human skin DCs with

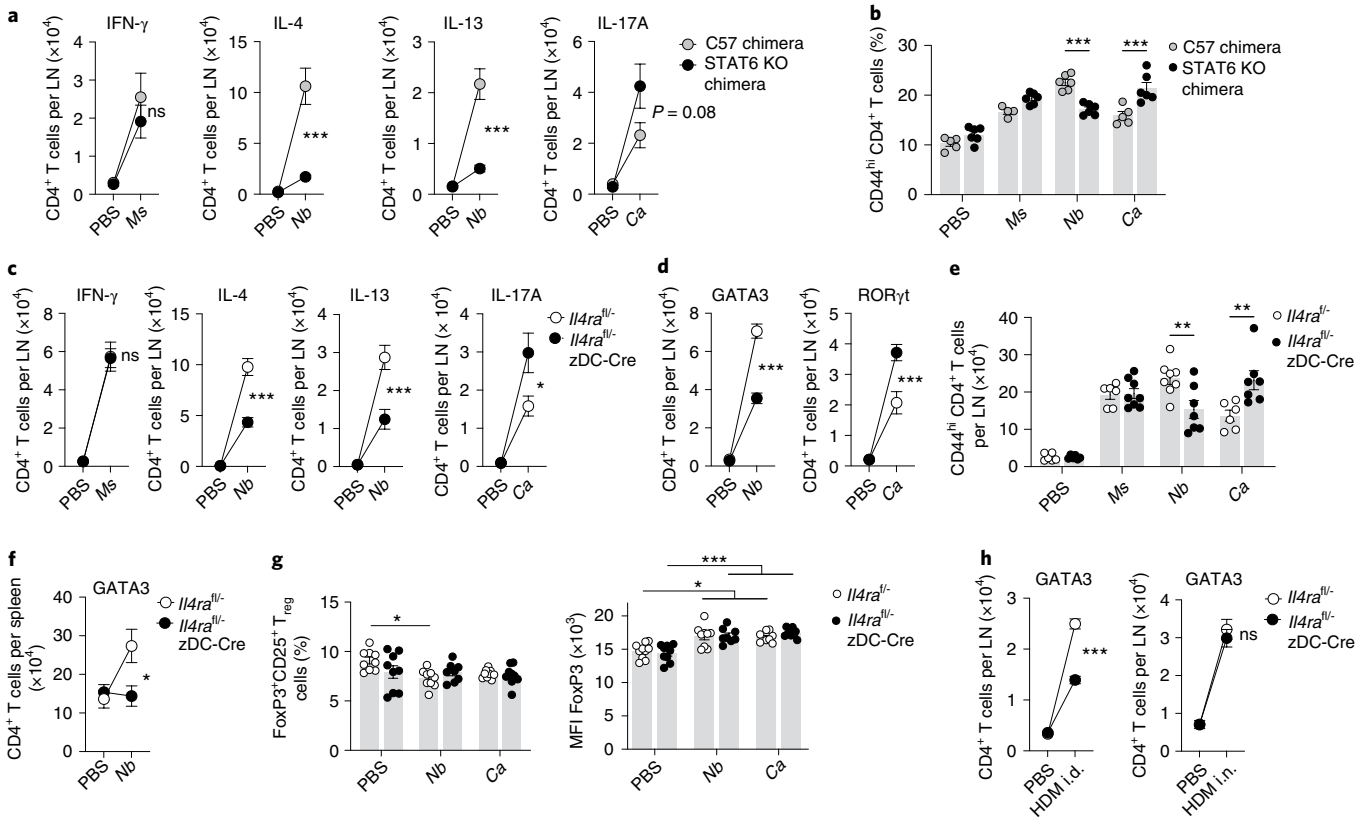

Fig. 6 | IL-13 signaling in DCs is required for optimal IL-4⁺ and IL-13⁺ CD4⁺ T cell responses in skin, but not lung, draining LNs. a,**b**, Numbers of cytokine-expressing (**a**) and frequencies of CD44^{hi} (**b**) CD45.1/CD45.2⁺CD4⁺ T cells in skin dLNs of C57 and STAT6 KO BM chimeras 5 days after intradermal (i.d.) immunization with *Ms*, *Nb* L3 larvae, *Ca*, or PBS as a control. Cells were stimulated with PMA and ionomycin before staining. **c**, Numbers of cytokine-expressing CD4⁺ T cells in the skin dLN of *Il4ra*$^{f/-}$ and *Il4ra*$^{f/-}$ zDC-Cre mice 5 days after i.d. immunization with *Ms*, *Nb*, *Ca* or PBS as a control. Cells were stimulated with PMA and ionomycin before staining. **d**,**e**, Numbers of RORγt⁺, GATA3⁺ (**d**) and CD44^{hi} (**e**) CD4⁺ T cells in the skin dLN of *Il4ra*$^{f/-}$ and *Il4ra*$^{f/-}$ zDC-Cre male mice 5 days after i.d. immunization with *Ms* (CD44 only), *Nb*, *Ca* or PBS. **f**, Numbers of GATA3⁺CD4⁺ T cells in the spleen of *Il4ra*$^{f/-}$ and *Il4ra*$^{f/-}$ zDC-Cre mice 5 days after i.d. immunization with *Nb* or PBS. **g**, Frequencies of FoxP3⁺CD25⁺CD4⁺ T cells and MFI of their FoxP3 expression in CD4⁺ T cell populations from the skin-dLN of *Il4ra*$^{f/-}$ and *Il4ra*$^{f/-}$ zDC-Cre mice 5 days after i.d. immunization with *Nb*, *Ca* or PBS. **h**, Numbers of GATA3⁺CD4⁺ T cells in the skin (left) or lung (right) dLN of *Il4ra*$^{f/-}$ and *Il4ra*$^{f/}$ zDC-Cre mice 5 days after i.d. or i.n. immunization with HDM extract or PBS. **a**,**c**,**d**,**f**,**h**, Symbols show mean ± s.e.m. and refer to $n = 4$–6 (**a** *Ms*, *Ca*), $n = 7$–10 (**a**, *Nb*), $n = 7$–12 (**c**), $n = 6$–9 (**d**,**f**) or $n = 10$–15 (**h**) mice pooled from two (**a**,**c** *Ms*, *Ca* and **d**,**f**,**h**) or three (**a**,**c** *Nb*) independent experiments. **b**,**e**,**g**, Bar graphs show mean ± s.e.m. for $n = 4$–6 (**b**,) $n = 6$–8 (**e**) or $n = 8$–9 (**g**) mice pooled from two independent experiments. Each symbol refers to one mouse. *P* values were determined using two-way ANOVA with Tukey's (**a**,**c**,**d**,**f**–**h**) or Sidak's (**b**,**e**) correction. $^*P < 0.05$; $^{**}P < 0.01$; $^{***}P < 0.001$; ns, nonsignificant; only relevant or significant comparisons are indicated.

blood or spleen DCs (Fig. 8a). GSEA enrichment plots for 'IL-4 and IL-13 signaling' genes further indicated that skin, but not lung, DC2s showed a significant enrichment for this pathway (Fig. 8b). Heatmaps showing expression of core-enrichment genes from the 'IL-4 and IL-13 signaling' pathway across the three microarray and one scRNA-seq studies revealed that similar transcripts were enriched in skin DC2 datasets compared with blood, spleen or lung DC2s (Fig. 8c and Extended Data Fig. 7a).

Expression of *IL13* transcripts was reported in human skin from healthy individuals[30,31]. To investigate whether this was associated with T cells or ILCs, we interrogated the dataset from one of these studies[30] for expression of IL-13 signaling genes in the immune and nonimmune skin cell compartments. As reported previously, we identified several clusters of myeloid cells, including monocytes, DC1s, DC2s, LCs and a small cluster of *CCR7*^{hi}/mature DCs (Fig. 8d and Extended Data Fig. 7b,c). Several genes that we identified as important for the IL-13-dependent development of DC2s in murine skin were also expressed in the human skin myeloid cell compartment, including *Il13RA1*, *IL4R*, *STAT6* and *KLF4* (Fig. 8e and Extended Data Fig. 7d). We also identified four lymphocyte clusters including ILCs (*CD3*$^-$*KLRD1*$^-$*IL7R*^{hi}*KLRB1*$^+$) (Fig. 8f). Cells within the ILC cluster expressed *KIT*, *IL2RA*, *GATA3*, which have been associated with KIT⁺ ILC3s and KIT^{int}IL2RA⁺GATA3⁺ILC2s (ref. [32]). *IL13* expression was detected at low levels in 5.12% and 2.96% of the T cell and ILC clusters in healthy skin, respectively (Fig. 8f,g). By contrast, only T cells but not ILCs expressed *IL4* (Fig. 8f,g). These analyses suggests that DC2s in healthy adult human skin are exposed to IL-13.

Discussion

We report that the steady-state production of IL-13 in murine dermis is necessary for the differentiation of a population of CD11b^{lo} dermal DC2s that is unique to skin. We show that the response of DC2s to IL-13 signaling requires expression of the transcription factors STAT6 and KLF4, thus explaining the specific requirement for KLF4 in CD11b^{lo} DC2 development[9]. We also show that dermal DC2s from healthy humans express an IL-4/IL-13 transcriptional signature, suggesting that human and mouse DCs are both exposed to IL-13 in the steady state. The ability of DC2s to sense IL-13 is functionally consequential and results in enhanced T_H2 and reduced T_H17 responses in mice.

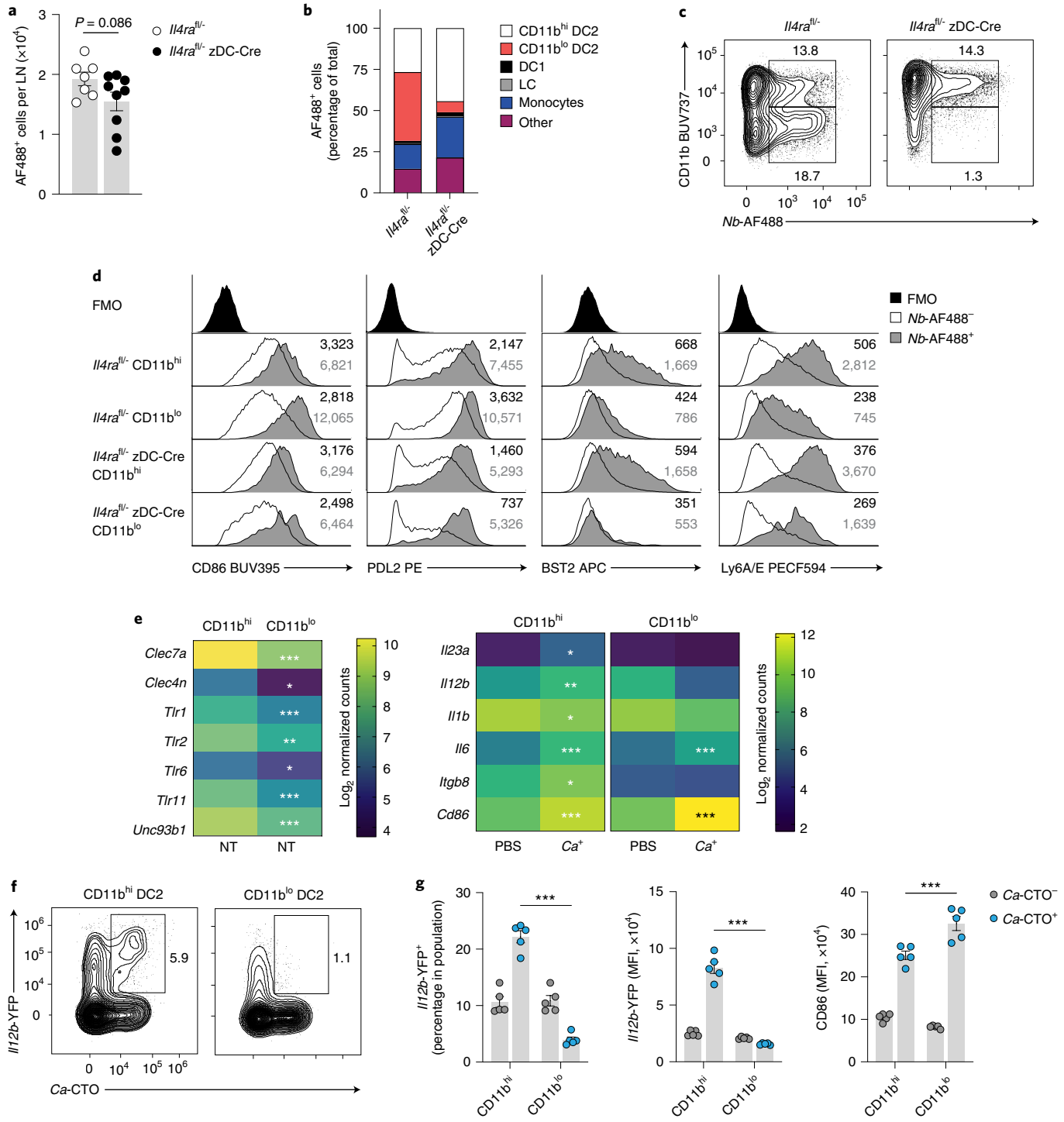

Fig. 7 | CD11b^{hi} and CD11b^{lo} DC2s are differentially activated by allergens and fungal antigens. a, Numbers of AF488$^+$ cells in the skin dLN of *Il4ra*$^{f/-}$ and *Il4ra*$^{f/-}$ zDC-Cre mice 48 h after intradermal (i.d.) immunization with AF488-labeled *Nb* (*Nb*-AF488). **b**, Frequencies of AF488$^+$ populations in the skin dLN of *Il4ra*$^{f/-}$ and *Il4ra*$^{f/-}$ zDC-Cre mice. Data refer to the experiments in **a**. **c**, *Nb*-AF488 uptake by DC2 populations in the skin dLN of *Il4ra*$^{f/-}$ and *Il4ra*$^{f/-}$ zDC-Cre mice. Data refer to the experiments in **a**. **d**, Phenotype of *Nb*-AF488$^-$ and *Nb*-AF488$^+$ DC2 populations from the skin dLNs of *Il4ra*$^{f/-}$ and *Il4ra*$^{f/-}$ zDC-Cre mice 48 h after i.d. immunization with *Nb*-AF488. Data are concatenated from three mice in one of two independent experiments that gave similar results. MFIs are indicated for each population. **e**, Expression of selected transcripts in total or *Ca*$^+$ DC2 subsets from the skin dLN of naive (NT) or *Ca*-immunized C57BL/6 mice 48 h after immunization as determined by bulk RNA sequencing. *P* values were calculated by DESeq2 and refer to the comparison with CD11b^{hi} DC2s (*Tlr* heatmap) or the respective PBS groups (cytokine heatmaps). **f**, Expression of *Il12b*-YFP in *Ca*-CTO$^-$ and *Ca*-CTO$^+$ DC2 populations from the skin dLN 48 h after *Ca*-CTO immunization. The *Ca*-CTO$^+$ *Il12b*-YFP$^+$ populations are highlighted. **g**, Expression and MFIs of *Il12b*-YFP reporter and CD86 MFIs in DC2 subsets from mice immunized with CTO-labeled *Ca* (*Ca*-CTO). Skin dLNs were examined 48 h after immunization. **a**,**g**, Bar graphs show mean ± s.e.m. for $n = 7$–9 (**a**) or $n = 5$ male (**g**) mice pooled from two independent experiments. Each symbol refers to one mouse. *P* values were determined using a two-tailed Student's *t*-test (**a**) or two-way ANOVA with Tukey's correction (**g**). ***$P < 0.001$. Only relevant comparisons are indicated.

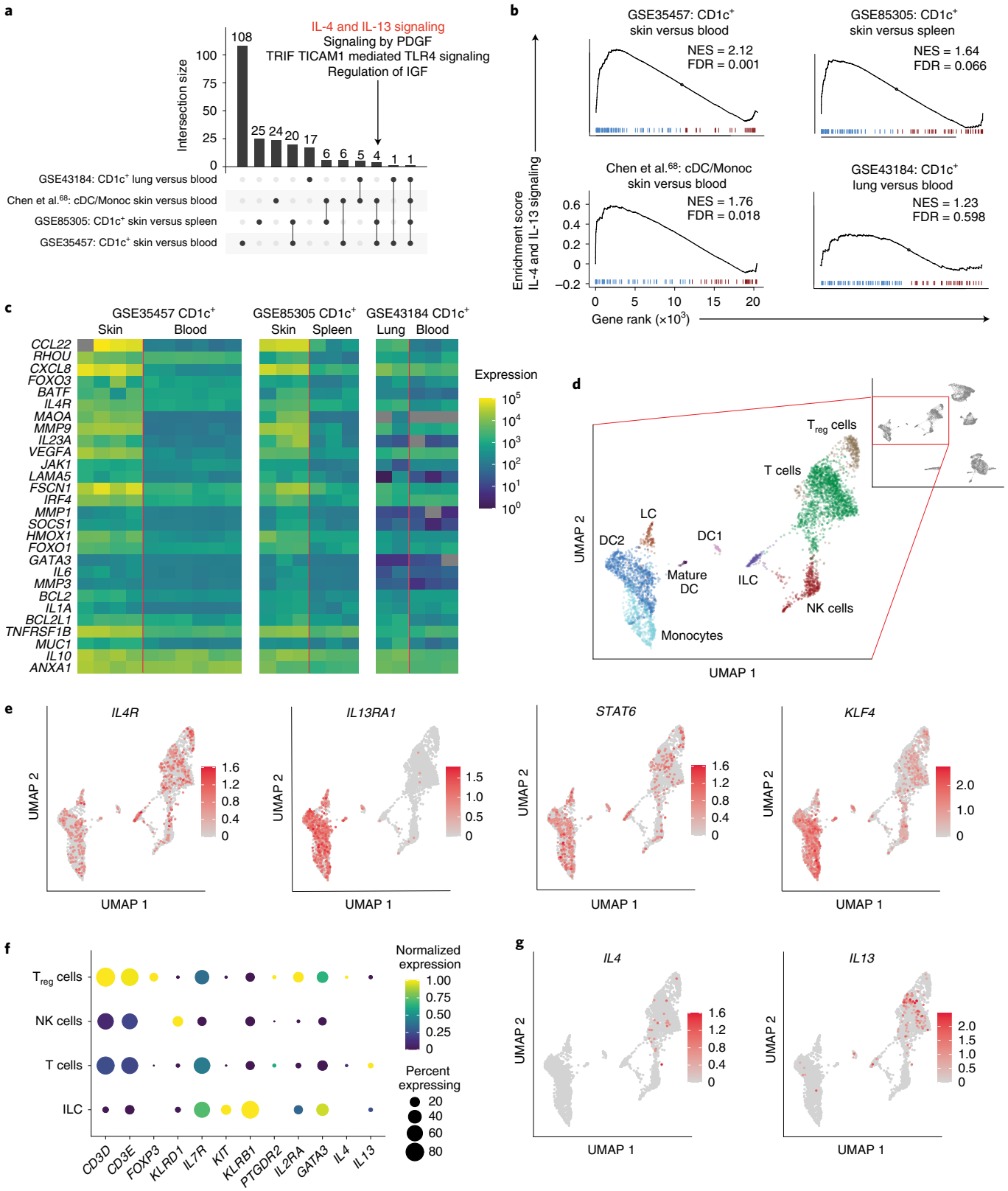

The heterogeneity of the DC2 subset across different tissues is presumably driven by tissue-specific signals that remain often uncharacterized[7]. Low levels of IL-13 in healthy skin were previously reported[13], raising the question of a potential homeostatic function for this cytokine[33]. Here we provide evidence that ILC2s and homeostatic IL-13 play an important role in the skin immune environment by supporting dermal DC2 differentiation at steady state. We also show that the proportion of CD11b^{lo} DC2s in skin and dLN is susceptible to regulation via IL-13 production by ILCs, with the reported lower IL-13 expression in male compared with female ILC2s[34] resulting in reduced frequencies of CD11b^{lo} DC2s in males. Perturbations of the skin environment that impair

Fig. 8 | IL-4/IL-13 signature genes are enriched in the transcriptome of DC2s from human skin, but not lung. a, UpSet plot showing the numbers of Reactome pathways that are enriched in the transcriptome of published datasets from CD1c+ DC2s from lung versus blood, and CD1c+ DC2s or DCs and monocytes from skin versus blood or spleen, as determined by GSEA. All samples were from healthy donors. The four pathways enriched only in skin samples are listed. IGF, insulin-like growth factor; PDGF, platelet-derived growth factor; TICAM1 (alias TRIF), TIR domain-containing adaptor molecule 1 (TIR domain-containing adaptor inducing interferon-β). **b**, GSEA enrichment plots of IL-4 and IL-13 signaling pathway genes in human tissue DC2s compared with blood or spleen as described in **a**. **c**, Heatmaps showing expression of GSEA core-enrichment genes from the IL-4 and IL-13 Reactome pathway in human CD1c+ DC2s from healthy donors in the indicated microarray studies. **d**, Detail of a UMAP plot showing lymphocyte and myeloid cell clusters from scRNA-seq data of skin biopsies and suction blisters from healthy controls (GSE153760). NK, natural killer. The full UMAP plot in gray includes all the clusters and can be found in Extended Data Fig. 7. **e**, Feature plots of the UMAP clusters in **d** showing the expression levels of *IL4R*, *IL13RA1*, *STAT6* and *KLF4* transcripts. Color intensity represents the level of normalized gene expression. **f**, Dotplot showing the expression of discriminatory markers for the different lymphocyte populations shown in **d**. **g**, Feature plots of the UMAP clusters in **d** showing the expression levels of *IL4* and *IL13* transcripts. Color intensity represents the level of normalized gene expression.

ILC2 numbers or function, such as increased amounts of IFNs, IL-27 or IL-23[35–37] may have a similar impact on CD11b^{lo} DC2s. Conversely, it remains unclear whether IL-13 can solely drive the differentiation of CD11b^{lo} DC2s, as IL-13 was not sufficient to induce downregulation of CD11b on other DC2 populations in dermis, lung or SI. The known positioning of DC2s in the dermal layer of the skin[38], and the expression of dermal ILC markers[14] on the ILC population in our study, may suggest an important role of dermal structures such as the hair follicle and sebaceous glands. The notion that IL-13 is not the sole signal controlling the differentiation of dermal CD11b^{lo} DC2 is also compatible with the presence of a small population of CD11b^{lo} DC2s in STAT6 KO and IL-4Rα KO mice.

IL-13 is an essential mediator in the priming of T_H2 immune responses in lung and intestine. In lung, allergen or parasite protease-dependent tissue injury and the consequent production of IL-33 support ILC2 production of IL-13 and promote DC activation, migration to the dLN and recruitment of T_H2 cells in nonlymphoid tissue[39,40]. In human and murine gut, IL-13 or IL-4 produced by allergen-specific T_H2 cells condition local DCs to promote and sustain type 2 immunity to ingested antigens[41,42]. Our data suggest that these immune networks and requirement for protease activity are probably redundant in skin because, unlike lung and gut, skin ILC2s produce IL-13 at steady state independently of skin microbiota, TSLP, IL-33 and IL-25 (ref. [15]). Therefore, healthy skin fosters DC2 activation for T_H2 priming independently of allergen properties. We also show that, compared with CD11b^{hi} DC2s, the IL-13 dependent CD11b^{lo} DC2s are less responsive to microbial stimuli, including *Ms*[19] and *Ca*, and express lower levels of proinflammatory cytokines including *IL12a*, *Il12b* and *Il23a*. Within the context of a response to commensals, which was not investigated in this study, IL-13-dependent DC2 conditioning might promote equilibrium by preventing excessive production of IL-17A, and promoting T_H2 potential for tissue repair[43]. The preferential induction of T_H17 versus T_H2 responses by distinct DC2 subsets has been reported previously[44].

While a preferred route for allergic sensitization in humans has not been established, epidemiological studies suggest that delayed introduction of some foods to infants may increase the likelihood of allergy development by providing greater opportunity for contact through skin[45]. Similarly, genetic mutations that decrease skin barrier function are associated with increased incidence of allergic disease that is not limited to skin but extends to respiratory and food allergy[46,47]. Our study provides a potential mechanism for these observations by documenting an IL-13-dependent and tissue-specific conditioning of dermal DC2s that leads to a T_H2 bias. Although the precise signals enabling IL-13-conditioned DC2s to prime T_H2 responses remain unclear, the increased responsiveness of CD11b^{lo} DC2s to TSLP (ref. [48]), an epithelial cytokine with a known role in promoting T_H2 responses[49] may play a role in this process.

In conclusion, steady-state IL-13 production by dermal ILCs underpins the differentiation of a CD11b^{lo} DC2 subset that is unique to skin, and fosters the differentiation of mouse CD4+ T cells to an IL-4+ T_H2 phenotype while reducing T_H17 responses. The functional consequences of this circuit in humans, in which an IL-13-dependent signature in skin DC2s is also apparent, are yet to be characterized. However, genome-wide association studies showing the opposing impact of *IL13* gene polymorphisms in atopic dermatitis versus psoriasis[50], two skin diseases that are dominated by dysregulated T_H2 and T_H17 activation, respectively, suggest a similar control in humans and an important role for this mechanism in the propensity to disease.

Online content

Any methods, additional references, Nature Research reporting summaries, source data, extended data, supplementary information, acknowledgements, peer review information; details of author contributions and competing interests; and statements of data and code availability are available at https://doi.org/10.1038/s41590-021-01067-0.

Received: 28 May 2021; Accepted: 5 October 2021;
Published online: 18 November 2021

References

1. Eisenbarth, S. C. Dendritic cell subsets in T cell programming: location dictates function. *Nat. Rev. Immunol.* **19**, 89–103 (2019).
2. Guilliams, M. et al. Unsupervised high-dimensional analysis aligns dendritic cells across tissues and species. *Immunity* **45**, 669–684 (2016).
3. Hilligan, K. & Ronchese, F. Antigen presentation by dendritic cells and their instruction of CD4+ T helper cell responses. *Cell Mol. Immunol.* **17**, 587–599 (2020).
4. Guerin, A. et al. IRF4 haploinsufficiency in a family with Whipple's disease. *eLife* **7**, e32340 (2018).
5. Alcantara-Hernandez, M. et al. High-dimensional phenotypic mapping of human dendritic cells reveals interindividual variation and tissue specialization. *Immunity* **47**, 1037–1050.e1036 (2017).
6. Heidkamp, G. F . et al. Human lymphoid organ dendritic cell identity is predominantly dictated by ontogeny, not tissue microenvironment. *Sci. Immunol.* **1**, eaai7677 (2016).
7. Sichien, D., Lambrecht, B. N., Guilliams, M. & Scott, C. L. Development of conventional dendritic cells: from common bone marrow progenitors to multiple subsets in peripheral tissues. *Mucosal Immunol.* **10**, 831–844 (2017).
8. Miller, J. C. et al. Deciphering the transcriptional network of the dendritic cell lineage. *Nat. Immunol.* **13**, 888–899 (2012).
9. Tussiwand, R. et al. Klf4 expression in conventional dendritic cells is required for T helper 2 cell responses. *Immunity* **42**, 916–928 (2015).
10. Henri, S. et al. CD207+ CD103+ dermal dendritic cells cross-present keratinocyte-derived antigens irrespective of the presence of Langerhans cells. *J. Exp. Med.* **207**, 189–206 (2010).
11. McCormick, S. M. & Heller, N. M. Commentary: IL-4 and IL-13 receptors and signaling. *Cytokine* **75**, 38–50 (2015).
12. Schlitzer, A. et al. Identification of cDC1- and cDC2-committed DC progenitors reveals early lineage priming at the common DC progenitor stage in the bone marrow. *Nat. Immunol.* **16**, 718–728 (2015).

13. Roediger, B. et al. Cutaneous immunosurveillance and regulation of inflammation by group 2 innate lymphoid cells. *Nat. Immunol.* **14**, 564–573 (2013).
14. Kobayashi, T. et al. Homeostatic control of sebaceous glands by innate lymphoid cells regulates commensal bacteria equilibrium. *Cell* **176**, 982–997 e916 (2019).
15. Ricardo-Gonzalez, R. R. et al. Tissue signals imprint ILC2 identity with anticipatory function. *Nat. Immunol.* **19**, 1093–1099 (2018).
16. Oliphant, C. J. et al. MHCII-mediated dialog between group 2 innate lymphoid cells and CD4(+) T cells potentiates type 2 immunity and promotes parasitic helminth expulsion. *Immunity* **41**, 283–295 (2014).
17. Naik, S. H. et al. Development of plasmacytoid and conventional dendritic cell subtypes from single precursor cells derived in vitro and in vivo. *Nat. Immunol.* **8**, 1217–1226 (2007).
18. Blecher-Gonen, R. et al. Single-Cell analysis of diverse pathogen responses defines a molecular roadmap for generating antigen-specific immunity. *Cell Syst.* **8**, 109–121 e106 (2019).
19. Hilligan, K. L. et al. Dermal IRF4+ dendritic cells and monocytes license CD4+ T helper cells to distinct cytokine profiles. *Nat. Commun.* **11**, 5637 (2020).
20. Lamiable, O., Mayer, J. U., Munoz-Erazo, L. & Ronchese, F. Dendritic cells in Th2 immune responses and allergic sensitization. *Immunol. Cell Biol.* **98**, 807–818 (2020).
21. Connor, L., Tang, S., Camberis, M., Le Gros, G. & Ronchese, F. Helminth-conditioned DC prime CD4+ T cells to IL-4 production in vivo. *J. Immunol.* **193**, 2709–2717 (2014).
22. Connor, L. M. et al. Th2 responses are primed by skin dendritic cells with distinct transcriptional profiles. *J. Exp. Med.* **214**, 125–142 (2017).
23. Harris, N. L., Peach, R. J. & Ronchese, F. CTLA4-Ig inhibits optimal T helper 2 cell development but not protective immunity or memory response to Nippostrongylus brasiliensis. *Eur. J. Immunol.* **29**, 311–316 (1999).
24. Pellefigues, C. et al. Toll-like receptor 4, but not neutrophil extracellular traps, promote IFN type I expression to enhance Th2 responses to *Nippostrongylus brasiliensis*. *Front. Immunol.* **8**, 1575 (2017).
25. Bojang, E., Ghuman, H., Kumwenda, P. & Hall, R. A. Immune sensing of *Candida albicans*. *J. Fungi (Basel)* **7**, 119 (2021).
26. Acharya, M. et al. αv Integrin expression by DCs is required for Th17 cell differentiation and development of experimental autoimmune encephalomyelitis in mice. *J. Clin. Invest.* **120**, 4445–4452 (2010).
27. Melton, A. C. et al. Expression of αvβ8 integrin on dendritic cells regulates Th17 cell development and experimental autoimmune encephalomyelitis in mice. *J. Clin. Invest.* **120**, 4436–4444 (2010).
28. Subramanian, A. et al. Gene set enrichment analysis: a knowledge-based approach for interpreting genome-wide expression profiles. *Proc. Natl Acad. Sci. USA* **102**, 15545–15550 (2005).
29. Jassal, B. et al. The reactome pathway knowledgebase. *Nucleic Acids Res.* **48**, D498–D503 (2020).
30. Rojahn, T. B. et al. Single-cell transcriptomics combined with interstitial fluid proteomics defines cell type-specific immune regulation in atopic dermatitis. *J Allergy Clin Immunol* **146**, 1056–1069 (2020).
31. He, H. et al. Single-cell transcriptome analysis of human skin identifies novel fibroblast subpopulation and enrichment of immune subsets in atopic dermatitis. *J. Allergy Clin. Immunol.* **145**, 1615–1628 (2020).
32. Teunissen, M. B. M. et al. Composition of innate lymphoid cell subsets in the human skin: enrichment of NCR(+) ILC3 in lesional skin and blood of psoriasis patients. *J. Invest Dermatol* **134**, 2351–2360 (2014).
33. Strid, J., McLean, W. H. I. & Irvine, A. D. Too much, too little or just enough: a Goldilocks effect for IL-13 and skin barrier regulation? *J. Invest. Dermatol.* **136**, 561–564 (2016).
34. Laffont, S. et al. Androgen signaling negatively controls group 2 innate lymphoid cells. *J. Exp. Med.* **214**, 1581–1592 (2017).
35. Bielecki, P. et al. Skin-resident innate lymphoid cells converge on a pathogenic effector state. *Nature* **592**, 128–132 (2021).
36. Moro, K. et al. Interferon and IL-27 antagonize the function of group 2 innate lymphoid cells and type 2 innate immune responses. *Nat. Immunol.* **17**, 76–86 (2016).
37. Duerr, C. U. et al. Type I interferon restricts type 2 immunopathology through the regulation of group 2 innate lymphoid cells. *Nat. Immunol.* **17**, 65–75 (2016).
38. Ronchese, F., Hilligan, K. L. & Mayer, J. U. Dendritic cells and the skin environment. *Curr. Opin. Immunol.* **64**, 56–62 (2020).
39. Halim, T. Y. et al. Group 2 innate lymphoid cells license dendritic cells to potentiate memory TH2 cell responses. *Nat. Immunol.* **17**, 57–64 (2016).
40. Halim, T. Y. et al. Group 2 innate lymphoid cells are critical for the initiation of adaptive T helper 2 cell-mediated allergic lung inflammation. *Immunity* **40**, 425–435 (2014).
41. Alpan, O., Bachelder, E., Isil, E., Arnheiter, H. & Matzinger, P. 'Educated' dendritic cells act as messengers from memory to naive T helper cells. *Nat. Immunol.* **5**, 615–622 (2004).
42. Zhou, X. et al. A positive feedback loop reinforces the allergic immune response in human peanut allergy. *J. Exp. Med.* **218**, e20201793 (2021).
43. Harrison, O. J. et al. Commensal-specific T cell plasticity promotes rapid tissue adaptation to injury. *Science* **363**, eaat6280 (2019).
44. Durai, V. & Murphy, K. M. Functions of murine dendritic cells. *Immunity* **45**, 719–736 (2016).
45. Du Toit, G. et al. Early consumption of peanuts in infancy is associated with a low prevalence of peanut allergy. *J. Allergy Clin. Immunol.* **122**, 984–991 (2008).
46. Irvine, A. D., McLean, W. H. & Leung, D. Y. Filaggrin mutations associated with skin and allergic diseases. *N. Engl. J. Med.* **365**, 1315–1327 (2011).
47. McAleer, M. A. & Irvine, A. D. The multifunctional role of filaggrin in allergic skin disease. *J. Allergy Clin. Immunol.* **131**, 280–291 (2013).
48. Ochiai, S. et al. CD326(lo)CD103(lo)CD11b(lo) dermal dendritic cells are activated by thymic stromal lymphopoietin during contact sensitization in mice. *J. Immunol.* **193**, 2504–2511 (2014).
49. Ziegler, S. F. Thymic stromal lymphopoietin and allergic disease. *J. Allergy Clin. Immunol.* **130**, 845–852 (2012).
50. Baurecht, H. et al. Genome-wide comparative analysis of atopic dermatitis and psoriasis gives insight into opposing genetic mechanisms. *Am. J. Hum. Genet* **96**, 104–120 (2015).

Methods

Ethics. For experiments performed in New Zealand, experimental protocols were approved by the Victoria University of Wellington Animal Ethics Committee. Experiments at the National Institute of Allergy and Infectious Diseases (NIAID) were approved by the NIAID Animal Care and Use Committee, and experiments at the University of Manchester were performed under license of the United Kingdom Home Office and under approved protocols at the University of Manchester. All experiments were performed according to institutional guidelines

Mice. The following mice were bred and housed under specific pathogen-free conditions, 21 ± 3 °C, 50 ± 10% humidity, 12 h/12 h light/dark cycle at the Malaghan Institute of Medical Research, Wellington, New Zealand:

C57BL/6J, BALB/cByJ, B6-SJ ptprca, CD11c-Cre (B6.Cg-Tg(Itgax-cre)1-1Reiz/J), IRF4-flox (B6.129S1-Irf4^{tm1Rdf}/J), STAT6 KO (B6.129S2(C)-Stat6^{tm1Gru}/J), zDC-Cre (B6.Cg-Zbtb46$^{tm3.1(cre)Mnz}$/J) and *Il12b*-YFP (B6.129-Il12b^{tm1Lky}/J) mice were from breeding pairs obtained originally obtained from the Jackson Laboratories. 4C13R reporters (Tg(Il4-AmCyan,Il13-DsRed*)1Wep), IL-4 KO (Il4$^{tm1.1Wep}$) and TSLPR KO (Crlf2^{tm1Wjl}) breeding pairs were provided by the late William Paul, NIAID, NIH; IL4Ra KO (Il4ra^{tm1Fbb}) and *Il4ra*$^{f/-}$ (Il4ra^{tm2Fbb}) breeders were from F. Brombacher, University of Capetown; MHCII KO (H2-Aa^{tm1Blt}) breeders were from the late Horst Blüthmann, Hoffman-La Roche Ltd; ST2 KO breeders (Il1rl1^{tm1Aki}) were from L. Mackay, University of Melbourne, Australia. *Itgax*-cre$^{+/-}$ *Irf4*$^{fl/fl}$ (*Irf4*$^{f/f}$ CD11c-Cre) and *Irf4*$^{fl/fl}$ (*Irf4*$^{f/f}$) mice were generated by crossing *Itgax*-cre to *Irf4*^{fl} mice for two generations. *zBTB46*-cre$^{+/-}$ *Il4ra*$^{f/-}$ (*Il4ra*$^{f/-}$ zDC-Cre) and *Il4ra*$^{fl/-}$ mice were generated by crossing *Zbtb*-cre females with *Irf4*^{fl} males for two generations.

For experiments at NIH, C57BL/6Tac and BALB/c were obtained from Taconic Biosciences, whereas B6.SJL-*Ptprc*^{a} *Pepc*^{b}/BoyJ, RAG1 KO on a C57BL6/J background and IL13Ra1 KO on a BALB/c background were from the NIAID contract facility at Taconic Biosciences and were maintained at 22 ± 3 °C 50 ± 20% humidity and a 14 h/10 h light/dark cycle. Germ-free C57BL/6 mice were bred and maintained in the NIAID Microbiome Program gnotobiotic animal facility.

CD4-Cre and iCOS-T (Icos$^{tm1.1(Hbegf)Anjm}$ CD4-Cre) mice were kindly provided by A. McKenzie, University of Cambridge, and were bred and maintained under specific pathogen-free conditions with 22 ± 2 °C, 55 ± 10% humidity and a 12 h/12 h light/dark cycle at the University of Manchester.

All mice were between 6 and 14 weeks of age and were age- and sex-matched within experiments. Female mice were used in all experiments unless otherwise indicated in figure legends.

Generation of IL-13 KO mice. IL-13 KO mice were generated by the Australian Phenomics Network and Monash Genome Modification Platform using the strategy illustrated in Supplementary Fig. 3b. CAS9 enzyme, guide RNA (gRNA) 1 targeting intron 1 (5′ - AGAGUCUUGGAGCUGAAAGA -3′) and gRNA2 targeting intron 3 (5′- CUUAGAGCGUUACAAGUCC- 3′) of the murine *Il13* gene were injected into C57BL/6 fertilized eggs to remove exons 2 and 3. Mice were screened for deletion by PCR using the primers P1 (5′-GAGGCTGGCATGGTGGTTTC-3′) and P2 (5′-TGGAGACCTGTGAAACGGCA-3′). Of two founder mice carrying exon 2–3 deletions, only one gave viable progeny carrying the mutation when crossed with C57BL/6. Mice were bred to homozygosity to generate IL-13 KO mice.

BM chimeras. BM cell suspensions were prepared by flushing cut femurs and tibias with unsupplemented IMDM (Gibco) and filtering through a sterile 70 µm cell strainer (Falcon). Recipient mice aged 10–12 weeks were treated with two doses of 5.5 Gy using a Gammacell 3000 Elan irradiator (MDS Nordion) given 3 h apart. One day after irradiation, mice received 1–8 × 10^6 BM cells from gender-matched donor mice as detailed in the text and figure legends.

For the generation of allogeneic mixed BM chimeras, BM donor mice were depleted of T cells by intraperitoneal (i.p.) injection of 200 µg InVivoMAb anti-mouse Thy-1 (Clone T24/31, InVivoPlus, BioXCell) on days −5 and −2 before BM collection. Recipient mice were injected with 100 µg anti-mouse Thy-1 i.p. 1 day after BM transfer. Chimeric mice were housed in individually ventilated cages and supplied with 2 mg ml^{-1} Neomycin trisulfate-supplemented drinking water for the first 3 weeks. Chimeras were left for at least 12 weeks before immunization.

Preparation of immunogens. *Ms* (mc2155) was grown in LB broth (Difco LB Lennox – low salt, BD) at 37 °C overnight. Bacteria were washed three times in PBS 0.05% Tween 80, heat-killed at 75 °C for 1 h and stored at −70 °C. *Nb* infective L3 larvae were prepared as described[19], washed three times with sterile PBS followed by three washes with antibiotic wash buffer (AWB: PBS supplemented with 100 µg ml^{-1} Gentamcycin (Sigma-Aldrich) and 500 U ml^{-1} Penicillin-Streptomycin (Gibco). Larvae were incubated in AWB twice for 1 h at room temperature, washed four times with sterile PBS and inactivated by three freeze-thaw cycles. *Ca* was propagated by inoculating sterile yeast extract-peptone-dextrose broth (Difco YPD, BD) and incubating at 30 °C for 72 h. Yeasts were washed in PBS and heat-killed at 75 °C for 1 h. HDM extract (Greer Laboratories Inc.) was reconstituted in sterile PBS to 10 mg dry weight per milliliter. For fluorescent labeling, inactivated *Nb* larvae were incubated in 0.05 M $NaHCO_3$ buffer and 0.1 mg AF488 NHS Ester (Molecular Probes, Invitrogen) for 15 min and washed with 0.1 M Tris buffer[19]. Inactivated *Ca* was labeled with CellTracker Orange CMTMR (CTO, Invitrogen, ThermoFisher Scientific) according to the manufacturer's instructions as previously described[19].

Immunizations and in vivo treatments. Mice were anesthetized with ketamine and xylazine (both Provet) and immunized intradermally in the ear with 4 × 10^6 colony-forming units (CFU) heat-killed *Ms*, 5–10 × 10^6 heat-killed *Ca*, or 300 nonviable *Nb* L3 larvae in 30 µl PBS[19]. HDM extract (200 µg) was injected intradermally in 30 µl PBS, or i.n. in 60 µl PBS; 20 µg of IL-13fp (Absolute Antibody) in 60 µl PBS was injected intraperitoneally on day 0, 10 µg IL-13fp was injected on days 2 and 3, and tissue collected on day 4. CD4-Cre and iCOS-T mice were treated with 1 µg of DT from *Corynebacterium diphtheriae* (DTx, Sigma) for 9 consecutive days by i.p. injection and tissues collected on day 10. Control mice were injected with the same volume of PBS.

Tissue sampling and processing. LNs were obtained, disrupted with 18 G needles and digested in IMDM containing 100 µg ml^{-1} liberase TL and 100 µg ml^{-1} DNase I (both Sigma-Aldrich) for 30 min at 37 °C. For skin preparations, ears were collected and split into ventral and dorsal halves, cut into small pieces and digested in 2 ml HBSS (Gibco) containing 2 mg ml^{-1} collagenase IV (Sigma-Aldrich) and 100 µg ml^{-1} DNase I (Sigma-Aldrich) for 30 min at 37 °C and 250 rpm in a shaking incubator. Lungs were collected after perfusion, cut into small pieces and digested in 1 ml IMDM (Gibco) containing 500 µg ml^{-1} liberase TL and 500 µg ml^{-1} DNase I (both Sigma-Aldrich) for 45 min at 37 °C and 150 rpm in a shaking incubator. Small intestinal segments were excised, Peyer's patches were removed and the intestines were opened longitudinally. Segments were then washed in PBS, cut into 0.5 cm pieces, collected in cold HBSS and washed twice with HBSS containing 2 mM EDTA (both Gibco) for 15 min at 37 °C and 200 rpm in a shaker to dissociate the epithelium. Segments were then digested in RPMI (Gibco) containing 10% FCS (Gibco), 1 mg ml^{-1} Collagenase VIII and 50 µg ml^{-1} DNase I (both Sigma-Aldrich) for 15–20 min at 37 °C and 200 rpm in a shaker. LN and spleen preparations for the assessment of T cell responses were generated by pressing the LNs. All cell suspensions were collected, filtered through a cell strainer, washed with FACS buffer (PBS supplemented with 2% FCS, 2 mM EDTA and 0.01% sodium azide (all Gibco)) and maintained at 4 °C. For the assessment of intracellular cytokines, single-cell suspensions were incubated in tissue culture medium (TCM, consisting of IMDM supplemented with 5% fetal calf serum (FCS), 1% penicillin-streptomycin and 55 µM 2-mercaptoethanol (all Gibco)) supplemented with 50 ng ml^{-1} PMA (Sigma-Aldrich), 1 µg;ml^{-1} ionomycin (Sigma-Aldrich) and 1 µl ml^{-1} GolgiStop (BD Pharmingen) for 5 h before surface and intracellular flow cytometry staining.

FLT3L BM cultures. BM cells were suspended in Red Blood Cell Lysing Buffer Hybri-Max (Sigma-Aldrich) for 1 min at room temperature, washed and resuspended in TCM supplemented with 4% FLT3L supernatant (generated from the cell line CHO flag Flk2.clone5 kindly provided by N. Nicola, WEHI). BM cells were cultured in six-well plates (Corning) at 5 × 10^6 per well in 5 ml TCM and incubated at 37 °C for 9 days. Cultures were fed every 3 days by removing 2 ml of medium and adding 2 ml of TCM containing 10% FLT3L supernatant. Murine rIL-13 (Peprotech) was added at different times and concentrations as indicated.

Phospho-STAT6 immunofluorescence. FLT3L BMDCs were obtained on day 9, resuspended at 1 × 10^6 ml^{-1} of TCM in 24-well plates and stimulated with 100 ng ml^{-1} murine rIL-13 (Peprotech) for 30 min at 37 °C. The cells (1 × 10^5) were then cytocentrifuged onto microscope glass slides (Trajan), fixed with 4% paraformaldehyde (ThermoFisher) for 10 min and permeabilized with 100% methanol at 4 °C for 10 min. We performed blocking for 1 h using SuperBlock T20 (ThermoFisher) before incubation with primary antibody (anti-pSTAT6 Tyr641 clone 46H1L12, ThermoFisher) for 1 h at 1:100 dilution in PBS and washing three times with PBS. Slides were then incubated with secondary antibody anti-rabbit Alexa Fluor 647 (ThermoFisher), anti-CD172a Alexa Fluor 594 (Biolegend) and 4,6-diamidino-2-phenylindole (DAPI) (0.5 µg ml^{-1}, Merck), washed three times and mounted. Fixation and staining were performed at room temperature. Images were obtained using the FV3000 confocal microscope (Olympus). Acquired images were first preprocessed with the FIJI imaging processing package (v.2.0.0-rc-69/1.52i (ref. [51])). Cell masks were generated using CellProfiler (v.4.0.3 (ref. [52])), while .fcs files were generated with Histocat (v.1.76 (ref. [53])). Gating and cell marker statistics were performed using Flowjo software (v.10.7, BD).

Flow cytometry and cell sorting. Single-cell suspensions were incubated in FACS buffer containing anti-mouse CD16/32 (clone 2.4G2, hybridoma culture supernatant, 1:300 dilution) before labeling with a mix of fluorescently labeled monoclonal antibodies for 30 min at 4 °C. Antibodies were used at a 1:200 dilution, unless otherwise indicated.

Antibodies from the following suppliers were used:

Biolegend: Anti-CD103 (clone 2E7), anti-CD11b (clone M1/70), anti-CD11c (clone N418), anti-CD124/IL-4Ra (clone I015F8), anti-CD3 (clone 145-2C11), anti-CD326/EpCAM (clone 1:1600), anti-CD4 (clone RM4-5), anti-CD44 (clone

IM7, 1:400), anti-CD45R/B220 (clone RA3-6B2), anti-CD86 (clone GL1), anti-IA/IE (clone M5/114.15.2, 1:400), anti-Ly6A/E (clone D7, 1:1000), anti-NK1.1 (clone PK136), anti-XCR1 (clone ZET).

BD Biosciences: Anti-CD117/c-kit (clone 2B8), anti-CD11c (clone HL3), anti-CD124/IL-4Ra (clone mIL4R-M1), anti-CD135/Flt3L (clone A2F10.1), anti-CD172/Sirpα (clone P84), anti-CD19 (clone 6D5), anti-CD200R3 (clone Ba13), anti-CD24 (clone 30-F1), anti-CD25 (clone 3C7), anti-CD26 (clone H194-112), anti-CD278/ICOS (clone 7E.17G9), anti-CD278/ICOS (clone C398.4 A), anti-CD317 (clone 927), anti-CD326/EpCAM (clone G8.8), anti-CD45 (clone 30-F11), anti-CD45.1 (clone A20), anti-CD45.2 (clone 104), anti-CD45R/B220 (clone RA3-6B2), anti-CD49b (clone DX5), anti-CD64 (clone X54-5/7.1), anti-CD8 (clone 2.43), anti-CD90.2 (clone 30-H12), anti-FcεRIα (clone MAR-1), anti-GATA3 (clone L50-823, 1:100), anti-IFN-γ (clone XMG1.2, 1:400), anti-IL-4 (clone 11B11, 1:100), anti-KLRG1 (clone 2F1), anti-Ly6C (clone AL-21, 1:1000), anti-Ly6C/Ly6G (clone RB6-8C5), anti-RORyt (clone Q31-378, 1:100), anti-TCRγδ (clone GL3).

ThermoFisher Scientific: Anti-CD11b (clone M1/70), anti-CD11c (clone N418), anti-CD127/IL-7Ra (clone A7R34), anti-CD172a/Sirpα (clone P84), anti-CD19 (clone ID3), anti-CD206 (clone MR6F3), anti-CD213a/IL-13Ra1 (clone 13MOKA, 1:100), anti-CD25 (clone PC6-1.5), anti-CD273/PDL2 (clone TY25), anti-CD3 (clone 145-2C11), anti-CD45R/B220 (clone RA3-6B2), anti-FoxP3 (clone FJK-16s, 1:100), anti-GATA3 (clone TWAJ), anti-IA/IE (clone M5/114.15.2, 1:400), anti-IL-13 (clone eBio13A, 1:100), anti-IL-17A (clone eBio17B7, 1:100), anti-IL33R/ST2 (clone RMST2-33, 1:100), anti-Ly6C/Ly6G (clone RB6-8C5), anti-Ly6G (clone 1A8), anti-NK1.1 (clone PK136), anti-Siglec H (clone eBio440c), anti-TCRβ (clone H57-597).

5-OP-RU-loaded MR1 tetramer conjugated to BV421 was generated at the NIH tetramer core facility and was kindly provided by O. Gasser.

Dead cells were excluded from analysis using DAPI (Molecular Probes), ZOMBIE NIR (Biolegend) or LIVE/DEAD Fixable Aqua (Molecular Probes).

For staining of intracellular cytokines, PMA + Ionomycin-stimulated cells were stained with LIVE/DEAD Fixable Blue (Molecular Probes) before staining of cell surface molecules. Cells were then fixed and permeabilized using a BD Cytofix/Cytoperm kit (BD Pharmingen) and stained with antibodies of relevant specificities.

For staining of transcription factors, cells were stained with LIVE/DEAD Fixable Blue (ThermoFisher) or LIVE/DEAD Fixable Aqua (Molecular Probes) before staining of cell surface molecules. Cells were then fixed and permeabilized using a True-Nuclear (BioLegend) or eBioscience Foxp3 (ThermoFisher) Transcription Factor Staining Buffer Set and stained and with antibodies of relevant specificities.

We performed sample acquisition on a LSR Fortessa or FACSymphony (both BD Biosciences) using BD FACS DIVA software or a 3L or 5L Aurora Spectral Flow Cytometer (Cytek Biosciences) using SpectroFlo software v.2.2. Final analysis and graphical output were performed using FlowJo (v.10.7, BD) or OMIQ (v.2020, OMIQ, Inc.) software.

Cell sorting was carried out using a BD INFLUX Cell sorter (BD Biosciences) and BD FACS software. Sorting of DC subsets for quantitative PCR with reverse transcription (RT-PCR) analysis was carried out after fluorescent labelling as described. DC2 subsets from skin dLN were identified as indicated in Supplementary Fig. 1, sorted directly into RNA lysis buffer (Zymo Research) and frozen at −80 °C until RNA extraction. Three biological replicates from individual mice were prepared in two separate DC sorting experiments. For sorting of DC subsets for RNA sequencing, cells were stained as described and presorted as $MHCII^{hi}$ migratory DCs from skin, lung and SI dLNs as indicated in Supplementary Fig. 1. Cells were resuspended in FACS buffer and the respective DC2 subsets were sorted directly into QIAzol Lysis Reagent (QIAGEN) and frozen at −80 °C until RNA extraction. Three biological replicates, each from five pooled mice, were prepared in three separate DC sorting experiments. For scRNA sequencing, cells were stained as described and a total of 26,000 SIRPα + DC2s per genotype were sorted from the pooled ear dLNs of three C57 and three STAT6 KO mice.

RNA isolation and bulk sequencing. Total RNA was prepared from frozen cell pellets using the RNeasy Micro Kit (QIAGEN). RNA was quantified using a Quantus Fluorometer (Promega) and RNA integrity was checked using a Fragment Analyzer (Agilent). Library preparation and RNA sequencing were contracted out to Otago Genomics, University of Otago. Ribosomal RNA was depleted using RiboZero (Illumina) before library preparation. We performed paired-end stranded RNA sequencing on an Illumina HiSeq 2500 V4 sequencing system using Illumina TruSeq kits. Between 10 and 30 million read pairs were generated per sample.

Read mapping and differential expression analysis for bulk RNA-seq. Paired-end raw FASTQ files were trimmed using Trimmomatic (v.0.36)[54] and aligned using STAR (v.2.7.1a)[55] to the *Mus musculus* mm10 M16 (GRCm38.p5) genome. Aligned reads were quality checked using MultiQC (v.1.7)[56] and counted using the R (v.3.4.4) package Rsubread (v.1.28.1)[57]. Differentially expressed genes were identified using the R package DESeq2 (v.1.28.1)[58] and the output was filtered for $\log_2$ fold change >1 in either direction and adjusted P values <0.05. VSTpk (variance-stabilized reads per thousand base pairs) values were generated from DESeq2 normalized counts using the DESeq2 Variance Stabilizing Transformation with default parameters, then dividing the resulting value by the length of the longest gene isoform in kilobases. Visualizations were made using the R packages pheatmap (v.1.0.12), UpSetR (v.1.4.0)[59] and Tidyverse (v.1.3.0).

TFBS analysis. For in silico prediction of TFBSs, the promoter sequences of the genes of interest (Table S1) were analyzed using TRANSFAC[60]. Sequences from 5,000 bp to 100 bp upstream (from −5,000 bp to +100 bp) of the transcription start site were selected and analyzed against a random set of genes of the same size with the immune cell specific group of matrices ($P < 0.01$, v.2020.02).

scRNA sequencing using BD Rhapsody. Sorted cells were labeled with sample tags from the Mouse Immune Single-Cell Multiplexing Kit (anti-mouse CD45, Clone 30-F11, BD Biosciences) following the manufacturer's instructions, washed, resuspended in BD Sample Buffer (BD Biosciences), counted, combined at 5,000 cells per genotype and loaded onto a BD Rhapsody nanowell cartridge followed by Capture Beads (BD Biosciences). After washing and cell lysis, the cell capture beads were retrieved for reverse transcription as per the manufacturer's protocol (BD Biosciences, Single-Cell Capture and cDNA Synthesis). cDNA Libraries were prepared using mRNA whole transcriptome analysis (WTA) and Sample Tag Library kits and Protocol (BD Biosciences), mRNA WTA and Sample Tag Library kits according to the manufacturer's instructions. The quality of the final libraries was assessed using a TapeStation 4150 (Agilent) with High Sensitivity D5000 ScreenTape and quantified using a Quantus Fluorometer (Promega). WTA and Sample Tag libraries were diluted to 4 nM and mixed together at a ratio of 99.63% WTA library to 0.37% cell multiplexing kit library. The libraries were loaded on an S1 flow cell (2 × 100 cycle) and paired-end sequenced at >200,000 reads per cell depth on a Novaseq 6000 Sequencer (Illumina) at the Kinghorn Centre for Cellular Genomics, Garvan Institute, Sydney, Australia. PhiX (20%) was added to the sequencing run to compensate for the low complexity library.

Analysis pipeline for scRNA-seq data. Paired-end raw FASTQ files were analyzed using FastQC/MultiQC[56]. Cell barcode correction and sample tag identification were performed using a custom script. We performed sample tag identification by mapping R2 reads to sample tag sequences using LAST V1066 (ref. [61]). Salmon Alevin v.1.4.0 (ref. [62]) was used for cell barcode detection, read mapping, unique molecular identifier (UMI) deduplication and gene count estimation. Data were analyzed using Seurat v.4 (ref. [63]) and Monocle3 (v.1.0.0)[64]. Differentially expressed markers with a fold change >1.5 in either direction and adjusted P value <0.05 between C57 and STAT6 KO cells within each cluster were identified using DESeq2.

Quantitative RT-PCR. RNA was extracted from 1,000 cells using the Quick-RNA Microprep Kit (Zymo Research) following the manufacturer's instructions. cDNA was synthetized from the total amount of extracted RNA using the high capacity RNA-to-cDNA kit (ThermoFisher). qPCR targets were preamplified using SsoAdvanced Preamp supermix (Bio-Rad) following the manufacturer's guidelines. As specified by the manufacturer's instructions, we diluted preamplified cDNA 40 times and performed quantitative RT-PCT (RT-qPCR) using SYBR Green Master Mix (ThermoFisher) and the forward (FW) and reverse (REV) primers (Integrated DNA Technologies) FW 5′-TGCTCAGGACCAGACCAATTC-3′ and REV 5′-CCTGGAAATCTCTGCAGGTGT-3′ for *Itgax*, FW 5′-CAGATCACACA TGCAACAGAGAC-3′ and REV 5′-TCAATTTCAAGCCCTTGCTGTG-3′ for *Ccl9*, FW 5′-TTCATGGACCTGCACAGGATG-3′ and REV 5′-GAAGTCTGCA GGGTTGTTGTG-3′ for *Abcg3*, FW 5′-GCGAGAAGATTCCGCTGGTA-3′ and REV 5′-CCGTTGACAGTCTTCCGACA-3′ for *Socs3*, FW 5′-GCCTGCACACC TCTACATCAT-3′ and REV 5′-CTGAGCATCCGTGAGTGGTG-3′ for *Sned1*, FW 5′-GCTGTGGGTGATGGACATGAT-3′ and REV 5′-TCCCTCAGAGGATGA TCCCG-3′ for *Khdc1a*, FW 5′-GCTACGCCGTCTACTGGAAC-3′ and REV 5′-AGTGAGGGCAGAAAACATCCA-3′ for *Efna5*, FW 5′-CTCTCTGGGCGAA ATCTGCT-3′ and REV 5′-GAGTGCTTTCGCTATGTTGTTCA-3′ for *Clmn* and FW 5′-TGATGGGTGTGAACCACGAG-3′ and REV 5′-GCCGTATTCATTGTC ATACCAGG-3′ for *Gapdh* using the Real-Time PCR System QuantStudio 7 instrument (Applied Biosystems) and QuantStudio Realtime PCR Software v.1.3. Transcript levels are expressed as the ratio of $2^{-\Delta CT}$(transcript of interest) to $^{2-\Delta CT}$(*Gapdh*).

Human DC2 transcriptomic data integration. The following microarray data were downloaded from GEO: human skin and blood DC2 (healthy volunteers)[65] from GSE35457, microarray data from adult human skin and spleen DC2 (healthy volunteers)[66] from GSE85305 and microarray data from human lung and blood DC2 (healthy volunteers)[67] from GSE43184. Microarray data were annotated using the 'illuminaHumanv4.db' R package (v.1.26.0). scRNA-seq data of human skin blister and blood cDC/monocytes from healthy volunteers[68] were obtained from the authors and normalized using the SCTransform function of Seurat v.3.2.0 (ref. [69]). To compare with the microarray data, gene expression for each group was summarized as the mean SCTransform expression across all cells within the group. Human skin blister cells and biopsy from healthy volunteers[30] were downloaded from GEO (GSE153760) and processed using Seurat v.3.2.0 (ref. [69]), following the v.3.2 'Integration and Label Transfer' vignette.

Gene set enrichment analysis. GSEA[28] and the Reactome database[29] were used to identify enriched signaling pathways in human DC2 from published microarray and scRNA-seq studies. Results from GSEA were processed using a custom script to recover cumulative per-marker scores for all ranked genes, so that they could be replotted with identical scales.

Quantification and statistical analyses. Statistical analyses were performed using Prism 9.1.2 (v.225, GraphPad) software. Number of samples, independent experiments and statistical tests used are indicated in figure legends. Data were analyzed using ordinary one-way analysis of variance (ANOVA) when comparing multiple groups, two-way ANOVA when comparing two variables or a two-tailed Student's *t*-test when comparing two groups as indicated in each figure legend. Tukey's and Sidak's multiple comparisons tests were applied as appropriate and are specified in each figure. Statistical significance was defined as $P < 0.05$.

For bulk and scRNA-seq experiments, genes differentially expressed between wild-type and STAT6 KO (fold change in either direction >2 for bulk RNA-seq and >1.5 for scRNA-seq, with adjusted *P* value <0.05) were identified using the R package DESeq2.

Reporting Summary. Further information on research design is available in the Nature Research Reporting Summary linked to this article.

Data availability

The authors declare that the data supporting the findings of this study are available within the paper and its supplementary information files or are available from the authors upon reasonable requests. Sequencing data generated for this study including bulk and scRNA-seq data presented in Figs. 1, 2 and Extended Data Fig. 2: raw RNA-seq data as FASTQ files have been deposited in NCBI SRA under bioproject PRJNA668222. IL-13 KO mice are available from G.L.G., MIMR upon request and pending approval of a Material Transfer Agreement. Source data are provided with this paper.

Code availability

All code and associated parameters used for the analysis of bulk and scRNA-seq data as well as the reanalysis of publicly available dataset in Fig. 8 are available at: https://doi.org/10.5281/zenodo.5534993.

References

51. Schindelin, J. et al. Fiji: an open-source platform for biological-image analysis. *Nat. Methods* **9**, 676–682 (2012).
52. Jones, T. R. et al. CellProfiler Analyst: data exploration and analysis software for complex image-based screens. *BMC Bioinf.* **9**, 482 (2008).
53. Schapiro, D. et al. histoCAT: analysis of cell phenotypes and interactions in multiplex image cytometry data. *Nat. Methods* **14**, 873–876 (2017).
54. Bolger, A. M., Lohse, M. & Usadel, B. Trimmomatic: a flexible trimmer for Illumina sequence data. *Bioinformatics* **30**, 2114–2120 (2014).
55. Dobin, A. et al. STAR: ultrafast universal RNA-seq aligner. *Bioinformatics* **29**, 15–21 (2013).
56. Ewels, P., Magnusson, M., Lundin, S. & Kaller, M. MultiQC: summarize analysis results for multiple tools and samples in a single report. *Bioinformatics* **32**, 3047–3048 (2016).
57. Liao, Y., Smyth, G. K. & Shi, W. The Subread aligner: fast, accurate and scalable read mapping by seed-and-vote. *Nucleic Acids Res.* **41**, e108 (2013).
58. Love, M. I., Huber, W. & Anders, S. Moderated estimation of fold change and dispersion for RNA-seq data with DESeq2. *Genome Biol.* **15**, 550 (2014).
59. Conway, J. R., Lex, A. & Gehlenborg, N. UpSetR: an R package for the visualization of intersecting sets and their properties. *Bioinformatics* **33**, 2938–2940 (2017).
60. Matys, V. et al. TRANSFAC and its module TRANSCompel: transcriptional gene regulation in eukaryotes. *Nucleic Acids Res.* **34**, D108–D110 (2006).
61. Hamada, M., Wijaya, E., Frith, M. C. & Asai, K. Probabilistic alignments with quality scores: an application to short-read mapping toward accurate SNP/indel detection. *Bioinformatics* **27**, 3085–3092 (2011).
62. Srivastava, A., Malik, L., Smith, T., Sudbery, I. & Patro, R. Alevin efficiently estimates accurate gene abundances from dscRNA-seq data. *Genome Biol.* **20**, 65 (2019).
63. Hao, Y. et al. Integrated analysis of multimodal single-cell data. *Cell* **184**, 3573–3587 (2021).
64. Cao, J. et al. The single-cell transcriptional landscape of mammalian organogenesis. *Nature* **566**, 496–502 (2019).
65. Haniffa, M. et al. Human tissues contain CD141hi cross-presenting dendritic cells with functional homology to mouse CD103+ nonlymphoid dendritic cells. *Immunity* **37**, 60–73 (2012).
66. McGovern, N. et al. Human fetal dendritic cells promote prenatal T-cell immune suppression through arginase-2. *Nature* **546**, 662–666 (2017).
67. Yu, C. I. et al. Human CD1c+ dendritic cells drive the differentiation of CD103+ CD8+ mucosal effector T cells via the cytokine TGF-beta. *Immunity* **38**, 818–830 (2013).
68. Chen, Y. L. et al. Re-evaluation of human BDCA-2+ DC during acute sterile skin inflammation. *J. Exp. Med.* **217**, jam.20190811 (2020).
69. Stuart, T. et al. Comprehensive integration of single-cell data. *Cell* **177**, 1888–1902 e1821 (2019).

Acknowledgements

We wish to thank G. Ogg, Oxford University, for sharing raw data of the scRNA-seq analysis of human skin blisters; P.M. Brunner and V. Vorstandlechner, Medical University of Vienna, for their advice on single-cell QC filtering and data analysis of scRNA-seq data of human skin biopsies and blisters cells; Y. Wang, Google, for developing the Shiny browser for scRNA-seq data and providing debugging help; M. Brewerton, Auckland DHB; A. Livingstone and T. Mosmann, University of Rochester; A. MacDonald, University of Manchester; S. Nutt, Walter and Eliza Hall Institute; and all colleagues at the Malaghan Institute of Medical Research for discussion and suggestions. The MR1 tetramer technology was developed jointly by J. McCluskey, J. Rossjohn and D. Fairlie, and the material was produced by the NIH Tetramer Core Facility as permitted to be distributed by the University of Melbourne, Australia. We also gratefully acknowledge the flow cytometry support of the members of the Hugh Green Cytometry Centre and the expert animal husbandry of the Biomedical Research Unit at the Malaghan Institute. This work was funded by an Independent Research Organization grant from the Health Research Council of New Zealand (HRC) to the Malaghan Institute (18-1003), an HRC Project grant to F.R. (18-510), and the Marjorie Barclay Trust. K.L.H. was supported by a Malaghan Institute Postdoctoral Fellowship and the Intramural Research Program of the NIAID, NIH. M.R.H. was supported by a Sir Henry Dale Fellowship jointly funded by the Wellcome Trust and the Royal Society (grant no. 105644/Z/14/Z), and a Lister Institute of Preventative Medicine Prize. R.G.D. was supported by an EMBO long-term fellowship (ALTF 1209-2019).

Author contributions

J.U.M., O.L. and F.R. conceived the study; J.U.M., O.L., K.L.H., J.S.C., R.G.D., J.Y., G.R.W., L.M.-E., K.A.W., E.J.H., S.-C.T., S.C.C., S.V.D. and L.M.C. designed, carried out and analyzed experiments; D.A.E. and S.I.O. carried out bioinformatics analyses, wrote code and visualized results; C.R.M., F.B., A.S., R.T., D.G.O., D.J. and G.L.G. provided essential reagents and/or expertise; O.L., A.S., M.R.H. and F.R. supervised and/or funded research; J.U.M., O.L. and F.R. wrote the original draft; J.U.M., O.L., K.L.H. and F.R. finalized the submission and revision with input from all authors. O.L. and F.R. prepared the final manuscript for publication.

Competing interests

The authors declare no competing interests.

Additional information

Extended data is available for this paper at https://doi.org/10.1038/s41590-021-01067-0.

Supplementary information The online version contains supplementary material available at https://doi.org/10.1038/s41590-021-01067-0.

Correspondence and requests for materials should be addressed to Franca Ronchese.

Peer review information *Nature Immunology* thanks Michel Gilliet, Daniel Kaplan and the other, anonymous, reviewer(s) for their contribution to the peer review of this work. Ioana Visan was the primary editor on this article and managed its editorial process and peer review in collaboration with the rest of the editorial team.

Reprints and permissions information is available at www.nature.com/reprints.

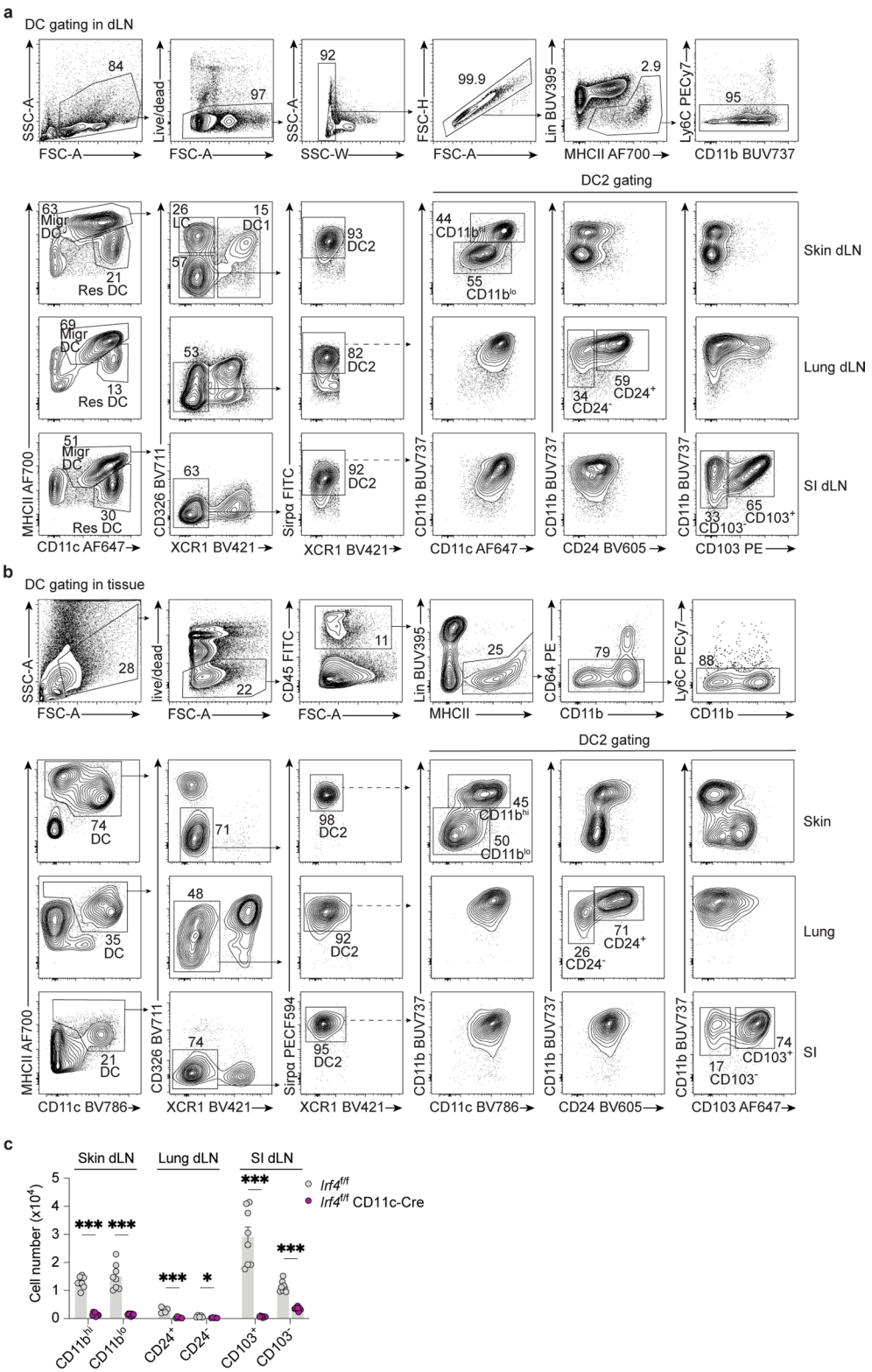

Extended Data Fig. 1 | Gating strategy for DC and DC2 populations in the skin, lung and small intestine of naive mice and their draining lymph nodes. **a**, Gating strategy for migratory DC2 subsets in skin, lung and small intestine (SI) dLNs. Generic gating on live single CD3⁻B220⁻Ly6G⁻ (Lin⁻) and Ly6C⁻ cells was performed for all samples before gating on dLN-specific DC2 subsets. **b**, Gating strategy for DC2 subsets in skin, lung and SI. Generic gating on live single CD45⁺CD3⁻B220⁻Ly6G⁻ (Lin⁻) and CD64⁻Ly6C⁻ cells was performed for all samples before gating on tissue-specific DC2 subsets. **c**, Numbers of DC2s in the skin, lung and SI dLN of *Irf4*$^{f/f}$ and *Irf4*$^{f/f}$ CD11c-Cre mice. Bar graphs show mean ± SEM for 5-8 mice pooled from 2 independent experiments. Each symbol refers to one mouse. *P* values were determined using a two-tailed Student's t-test. *$P < 0.05$; ***$P < 0.001$; only significant comparisons are indicated.

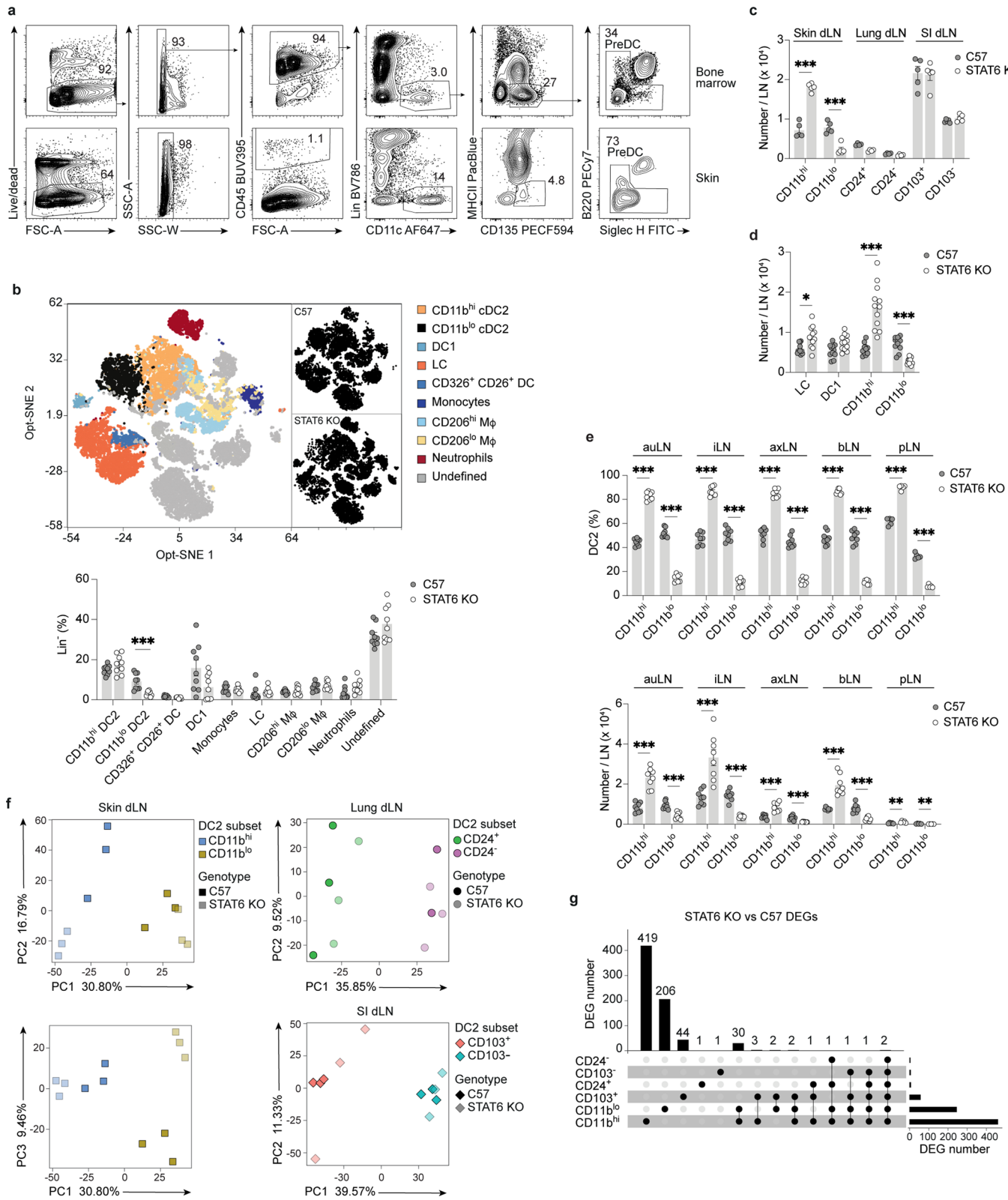

Extended Data Fig. 2 | See next page for caption.

Extended Data Fig. 2 | Phenotypic and transcriptomic characterization of myeloid and DC2 populations in C57BL/6 and STAT6 KO mice. a, Gating strategy for DC2 precursors in the bone marrow and skin. **b**, Representative Opt-SNE visualization of concatenated live single $CD45^+CD3^-CD19^-$ myeloid cells from the skin of naive C57BL/6 (C57) and STAT6 KO mice; combined data from both strains are shown in the color image. Opt-SNE was performed on 16648 events (2081 events/mouse, 4 mice per genoype, one experiment) using 12 parameters (XCR1, CD206, CD11b, Ly6c, CD11c, Ly6G, SIRPα, CD326, CD26, CD64, BST2, MHC-II) with default OMIQ settings and a perplexity of 30 with 1000 iterations. Population frequencies are shown in the bar graph. **c**, Numbers of migratory DC2s in the skin, lung and small intestine (SI) dLNs of naive C57 and STAT6 KO mice. **d**, Number of migratory DCs in the skin dLN of naive C57 and STAT6 KO mice. **e**, Relative frequencies (top) and numbers (bottom) of $CD11b^{hi}$ and $CD11b^{lo}$ DC2s in the auricular (au), inguinal (i), axillary (ax), brachial (b) and popliteal (p) skin dLNs of naive C57 and STAT6 KO mice. **f**, Principal component (PC) analyses of all expressed genes in DC2 subsets from the skin, lung and SI dLNs of naive C57 and STAT6 KO mice. Each symbol refers to a biological replicate. **g**, UpSet plot showing the numbers of unique and shared differentially expressed genes (DEGs, including up- and downregulated genes) in the indicated DC2 subsets from the skin, lung and SI dLNs of STAT6 KO vs. C57 mice. **b-e**, Bar graphs show mean ± SEM for n=9 (**b**) n=4-5 (**c**) n=9-10 (**d**) n=5-8 (**e**) mice pooled from 2 independent experiments. Each symbol refers to one mouse. *P* values were determined using a two-tailed unpaired Student's t-test. $^*P < 0.05$; $^{***}P < 0.001$; only significant comparisons are indicated.

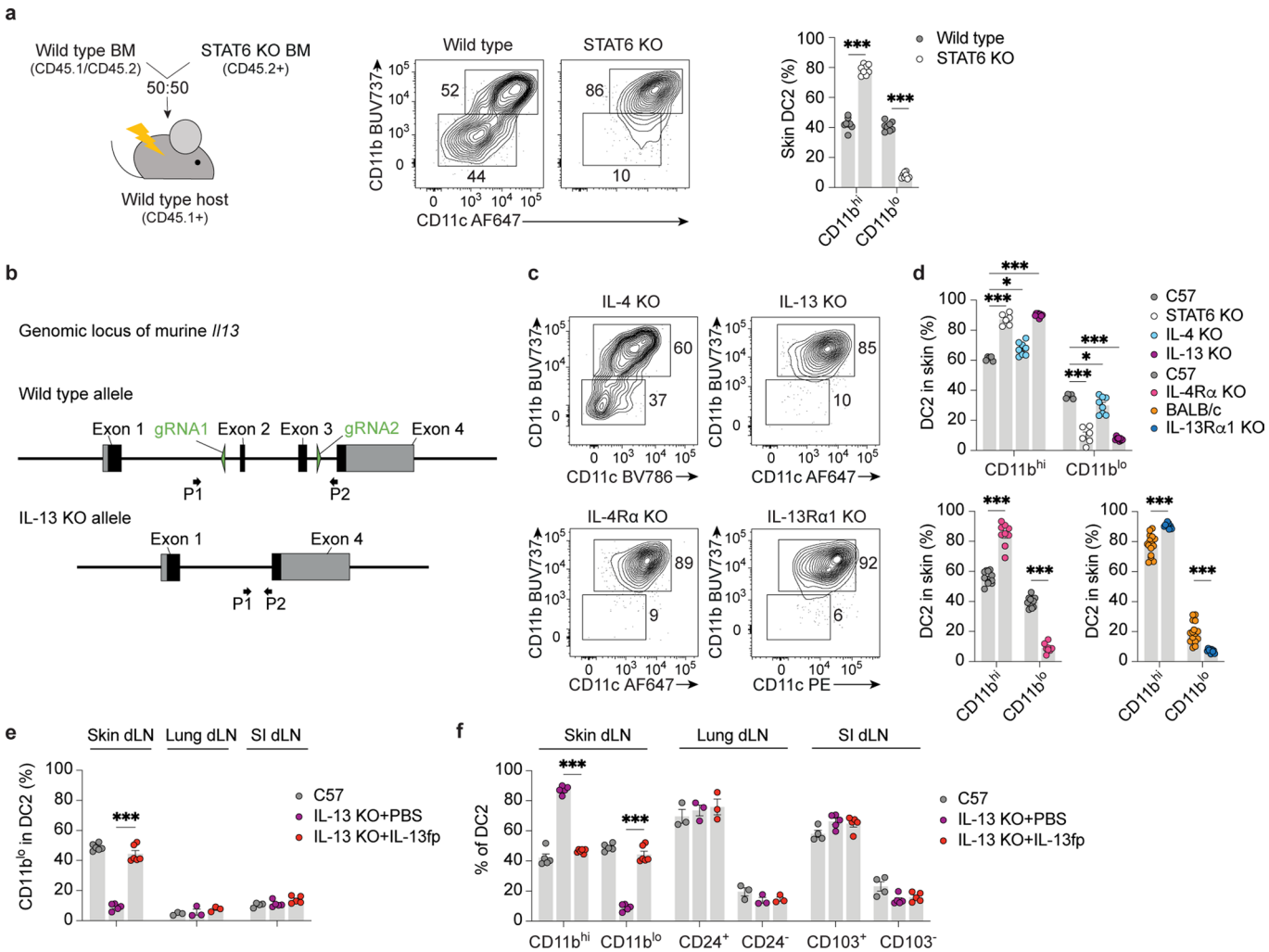

Extended Data Fig. 3 | IL-13 signalling is necessary for the development of CD11b^{lo} DC2s in skin. a, Experimental set-up of mixed wild type and STAT6 KO BM chimeras. The phenotype of skin DC2s from each donor BM is shown in the contour plots, subsets are quantified in the bar graph. **b**, Schematic of the genomic *Il13* locus in wild type and IL-13 KO mice illustrating the deletion of exons 2 and 3. **c**, Phenotype of skin DC2s in naive mice of the indicated strains. All KO strains were on a C57BL/6 background except for the IL-13Rα1 KO which were on a BALB/c background. **d**, Relative frequencies of skin DC2 subsets in naive mice of the indicated strains. **e,f**, Frequencies of CD11b^{lo} DC2s (**e**) and DC2 subsets (**f**) in DC2 populations from skin, lung and small intestine (SI) dLNs of C57 controls, and IL-13 KO mice treated with either PBS or IL-13 fusion protein (IL-13fp). In (**e**), C57 controls are representative of several repeats. **a,d,e,f**, Bar graphs shows mean ± SEM for n=8 (**a**) n=5-15 (**d**) n=3-6 (**e,f**) mice pooled from 2 (**a,d,e** IL-13 KO, f) or 1 (**e**, C57 lung and SI dLNs) independent experiments. Each symbol refers to one mouse. *P* values were determined using two-way ANOVA with Sidak's (**a**, lower graphs in **d**, IL-13 KO in **e,f**) or Tukey's (**d**, top graphs) correction $^{*}P < 0.05$; $^{***}P < 0.001$. Only relevant significant comparisons are indicated.

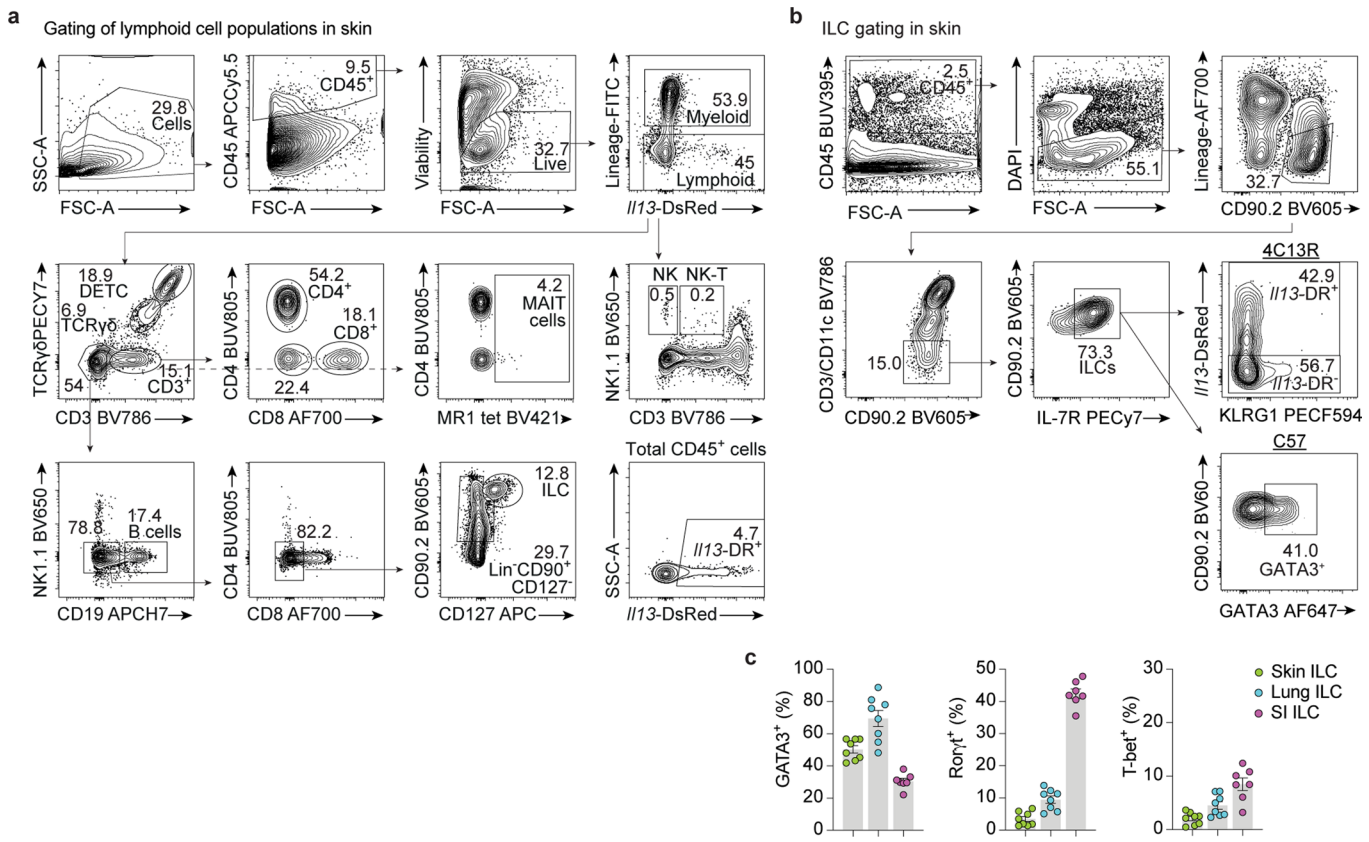

Extended Data Fig. 4 | Identification of lymphoid cell populations in murine skin. a, Gating strategy to identify lymphoid cell populations in the ear skin of naive 4C13R reporter mice. To define cells of lymphoid origin, cells were pre-gated on single, live, CD45$^+$, myeloid-lineage negative (CD11b$^-$Ly6G$^-$Ly 6C$^-$CD11c$^-$) cells. *Il13*-DsRed$^+$ cells were gated within each cell population, or in the total CD45$^+$ population as shown in the lower right panel. **b**, Gating strategy to identify innate lymphoid cells (ILCs) in the skin of naive 4C13R reporter or C57 mice. The Lineage AF4700 gate includes antibodies specific for B220, Ly6G, Ly6C, NK1.1, CD11b, and FCεRIα. A similar gating strategy was used to identify ILCs in lung and small intestine (SI). **c**, Frequencies of GATA3$^+$, RORγt$^+$, T-bet$^+$ ILCs in the skin, lung and SI of naive C57 mice. Bar graphs show mean ± SEM for 7-8 mice pooled from 2 independent experiments. Each symbol refers to one mouse.

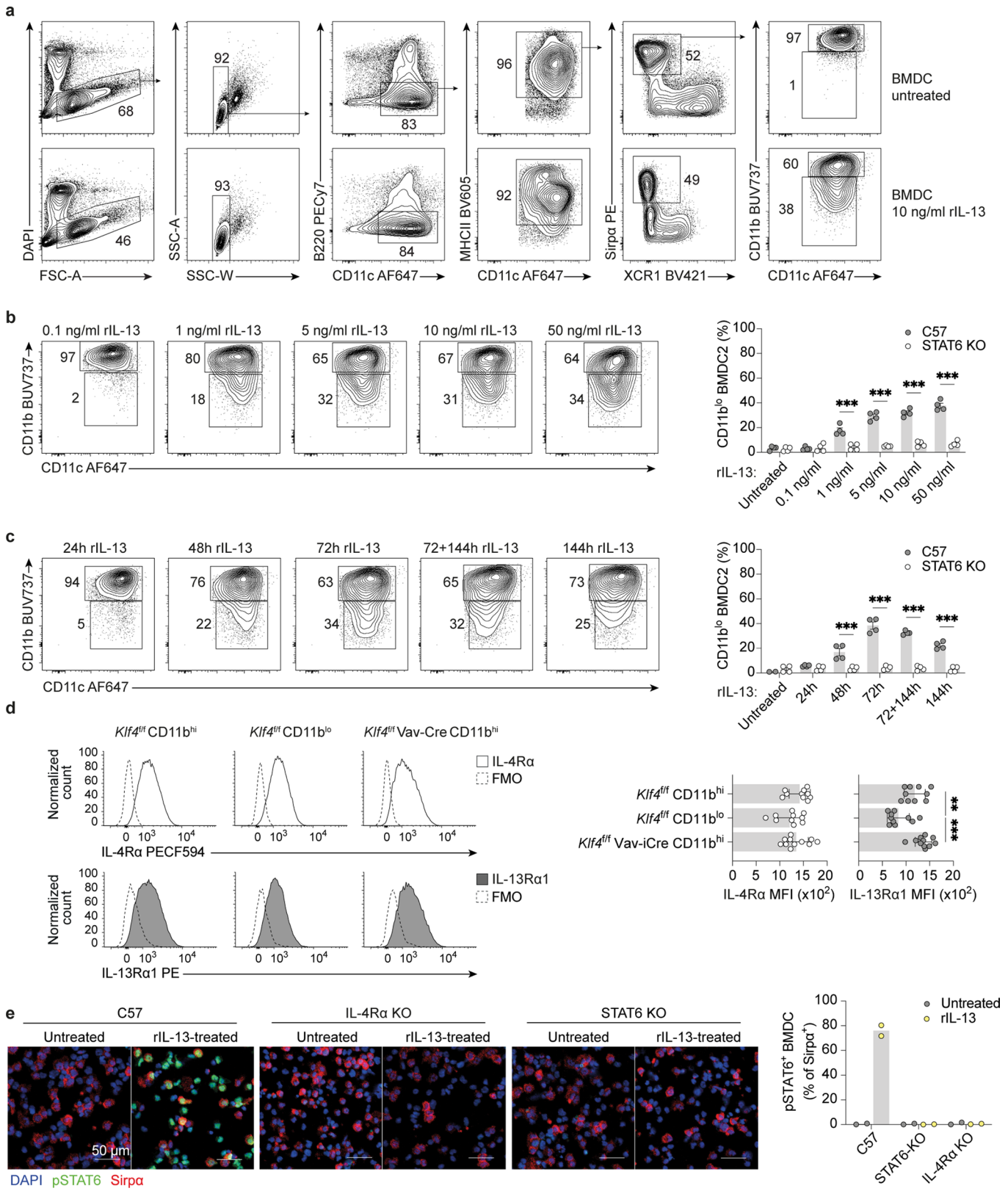

Extended Data Fig. 5 | See next page for caption.

Extended Data Fig. 5 | IL-13 signalling drives the development of CD11b^{lo} DC2 *in vitro* in a dose and time dependent manner. a, Gating strategy to identify Sirpα^{+} DC2 in FLT3L bone marrow DC (BMDC) cultures from C57BL/6 (C57) donors. Cultures were untreated or supplemented with 10 ng/ml rIL-13 for the last 72h of culture as indicated. **b**, Phenotype of Sirpα^{+} DC2 subsets in FLT3L BMDCs cultures from C57 donors. Cultures were treated with the indicated concentrations of rIL-13 for the last 72h. Frequencies of CD11b^{lo} DC2s are shown in the bar graph. **c**, Phenotype of Sirpα^{+} DC2 subsets in FLT3L BMDC cultures from C57 donors. Cultures were supplemented with 10 ng/ml rIL-13 at the indicated times before harvest. Frequencies of CD11b^{lo} DC2s are shown in the bar graph. **d**, IL-4Rα and IL-13Rα1 expression on DC2 subsets from the skin dLNs of male *Klf4*$^{f/f}$→C57 and *Klf4*$^{f/f}$ Vav1-iCre→C57 chimeric mice. FMO: fluorescence-minus-one. Histograms show concatenated data from 3 mice. Median fluorescence intensities (MFI) are reported in the bar graphs. **e**, Representative images of FLT3L BMDC cultures from male C57, IL-4Rα KO and STAT6 KO donors that were set up as controls for the experiments in Figure 5e. Cultures were either unstimulated or treated with 100 ng/ml rIL-13 for 30 minutes before staining. Scale bars correspond to 50 μm. Frequencies of pSTAT6^{+} cells in the Sirpα^{+} population are quantified in the bar graph. An average of 2200 Sirpα^{+} cells/sample were assessed. Each symbol refers to one culture from one of two repeat experiments. **b-d**, Bar graph shows mean ± SEM for n=4 (**b,c**) cultures or n=10-11 (**d**) mice pooled from 2 (**b,c**) or 3 (**d**) separate experiments. Each symbol refers to one independently treated culture or one mouse. *P* values were determined using two-way ANOVA with Sidak's correction (**b,c**) or one-way ANOVA with Tukey's correction (**d**). $^{**}P < 0.01$; $^{***}P < 0.001$; only significant comparisons are indicated.

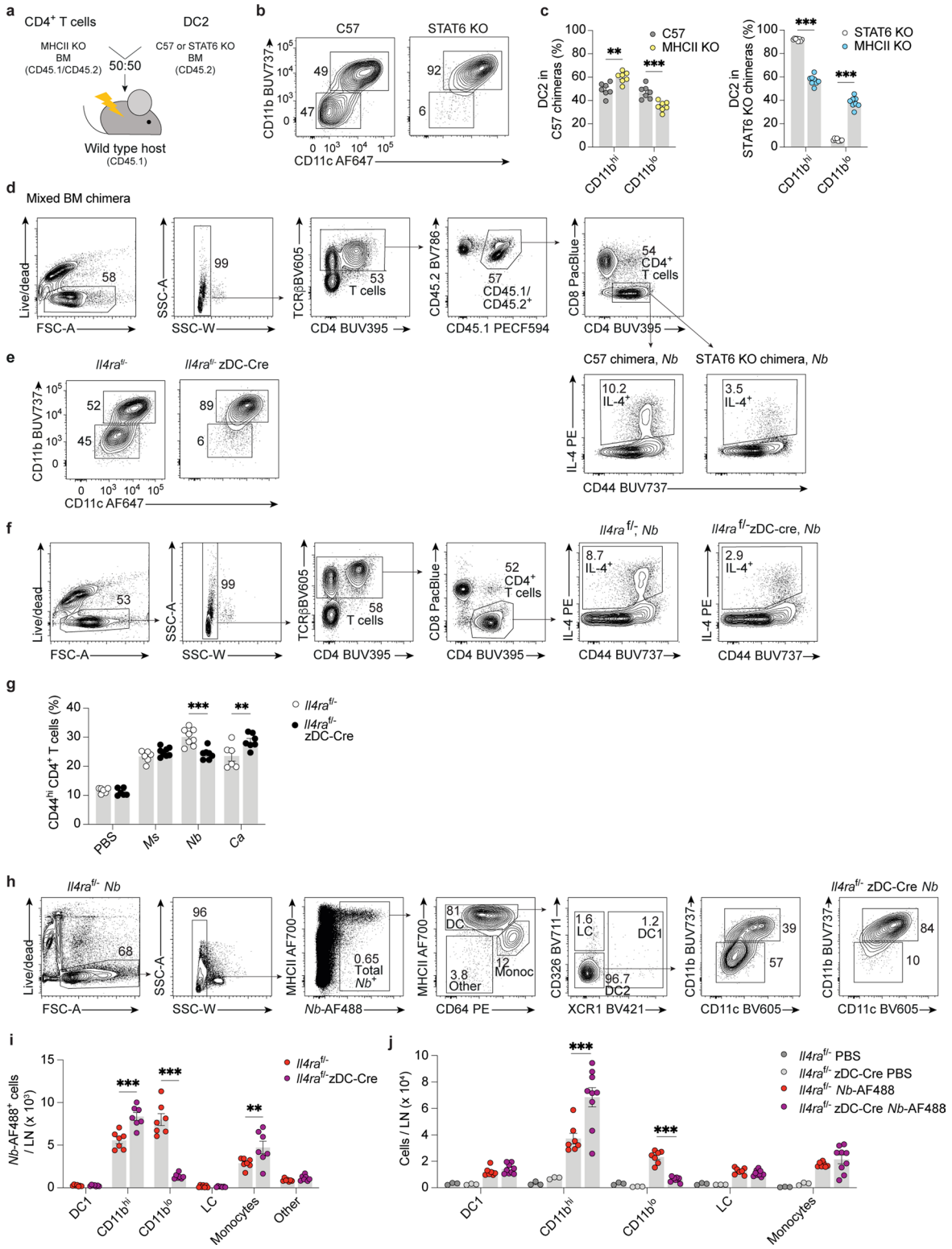

Extended Data Fig. 6 | See next page for caption.

Extended Data Fig. 6 | IL-13 signalling in DC2s is required for optimal IL-4$^+$ T_H responses in skin-draining lymph node. a, Experimental set-up of mixed bone marrow (BM) chimeras to compare the antigen-presenting function of C57 and STAT6 KO DCs. **b**, Phenotype of DC2 populations in the skin dLN of naive C57 and STAT6 KO chimeras. **c**, Relative frequencies of DC2 subsets from each donor BM in the skin dLN of naive C57 or STAT6 KO mixed BM chimeras. **d**, Gating strategy to identify cytokine-expressing CD45.1/CD45.2$^+$CD4$^+$ T cells in the skin dLN of *Nb*-immunized C57 or STAT6 KO mixed BM chimeras. Gating for IL-4$^+$CD4$^+$ T cells is shown; other cytokines were gated in a similar manner. **e**, Phenotype of DC2 subsets in the skin dLN of naive *Il4ra*$^{f/-}$ and *Il4ra*$^{f/-}$ zDC-Cre mice. **f**, Gating strategy to identify cytokine-expressing CD4$^+$ T cells in the skin dLN of *Nb*-immunized *Il4ra*$^{f/-}$ and *Il4ra*$^{f/-}$ zDC-Cre mice. Gating for IL-4$^+$ CD4$^+$ T cells is shown; other cytokines were gated in a similar manner. **g**, Frequencies of CD44^{hi}CD4$^+$ T cells in the skin dLN of *Il4ra*$^{f/-}$ and *Il4ra*$^{f/-}$ zDC-Cre mice 5 days after intradermal immunization with *Mycobacterium smegmatis* (*Ms*), *Nippostrongylus brasiliensis* L3 larvae (*Nb*), *Candida albicans* (*Ca*) or PBS as a control. **h**, Gating strategy for AF488$^+$ cells in the skin dLN of *Il4ra*$^{f/-}$ and *Il4ra*$^{f/-}$ zDC-Cre mice 48 hours after intradermal injection of AF488-labeled *Nb* (*Nb*-AF488). **i**, Numbers of AF488$^+$ cells in the skin dLN of *Il4ra*$^{f/-}$ and *Il4ra*$^{f/-}$ zDC-Cre mice 48 hours after intradermal injection of *Nb*-AF488. **j**, Numbers of total DCs and monocytes in the skin dLN of *Il4ra*$^{f/-}$ and *Il4ra*$^{f/-}$ zDC-Cre mice 48 hours after intradermal injection of *Nb*-AF488 or PBS. **c,g,i,j**, Bar graphs show mean ± SEM for n=7-8 (**c**) n=6-8 (**g**) n=7 (**i**) n=3-9 (**j**) mice pooled from 2 independent experiments. *P* values were determined using two-way ANOVA with Sidak's correction. $^{**}P < 0.01$; $^{***}P < 0.001$; only significant comparisons are indicated. Each symbol refers to one mouse.

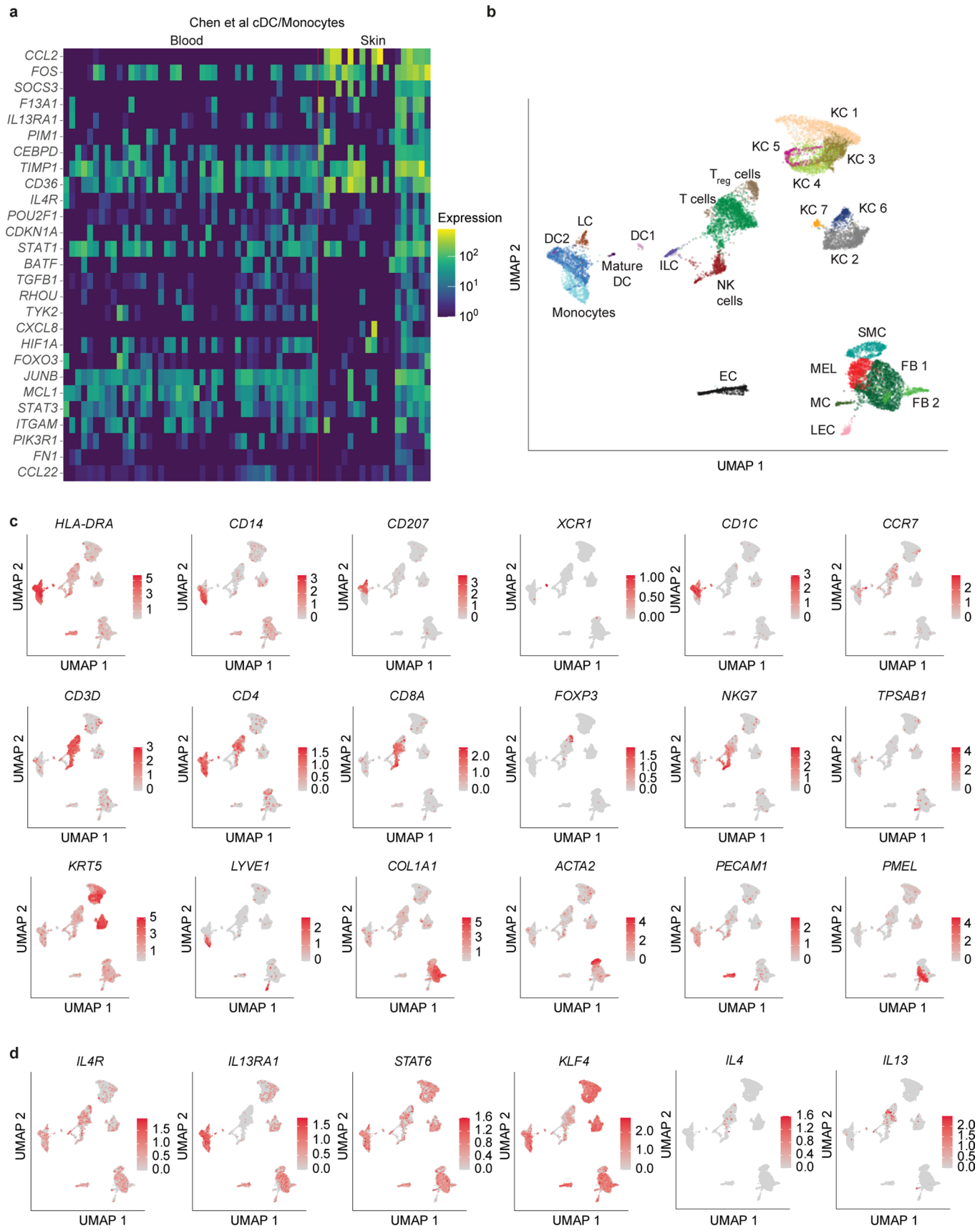

Extended Data Fig. 7 | See next page for caption.

Extended Data Fig. 7 | Enrichment of IL-4/IL-13 signature genes in DC2s from healthy human skin. a, Heatmap showing the expression of GSEA core-enrichment genes of the IL-4 and IL-13 Reactome pathway in cDCs and monocytes from the blood and skin of healthy donors from a published scRNA-seq dataset (Chen et al, 2020). **b**, UMAP plot showing scRNA-seq subclusters of cells from skin biopsies and suction blisters of healthy donors from the published dataset GSE153760. EC: Endothelial cells, FB 1, FB 2: Fibroblast clusters 1&2, ILC: Innate lymphoid cells, LC: Langerhans cells, LEC: Lymphatic endothelial cells, MC: Mast cells, MEL: Melanocytes, NK: Natural killer cells, KC 1-7: Keratinocyte clusters 1-7, SMC: Smooth muscle cells, T_{reg} cells: Regulatory T cells. **c**, Feature plots of the UMAP clusters in (**b**) showing the expression levels of cluster-specific transcripts used for cluster identification. Color intensity represents the level of normalized gene expression. **d**, Feature plots of the UMAP clusters in (**b**) showing expression levels of *IL4R*, *IL13RA1*, *STAT6*, *KLF4*, *IL4* and *IL13* transcripts. Color intensity represents the level of normalized gene expression.

nature research

Corresponding author(s): Franca Ronchese

Last updated by author(s): 30 September 2021

Reporting Summary

Nature Research wishes to improve the reproducibility of the work that we publish. This form provides structure for consistency and transparency in reporting. For further information on Nature Research policies, see our Editorial Policies and the Editorial Policy Checklist.

Statistics

For all statistical analyses, confirm that the following items are present in the figure legend, table legend, main text, or Methods section.

n/a	Confirmed	
☐	☒	The exact sample size (*n*) for each experimental group/condition, given as a discrete number and unit of measurement
☐	☒	A statement on whether measurements were taken from distinct samples or whether the same sample was measured repeatedly
☐	☒	The statistical test(s) used AND whether they are one- or two-sided *Only common tests should be described solely by name; describe more complex techniques in the Methods section.*
☒	☐	A description of all covariates tested
☐	☒	A description of any assumptions or corrections, such as tests of normality and adjustment for multiple comparisons
☐	☒	A full description of the statistical parameters including central tendency (e.g. means) or other basic estimates (e.g. regression coefficient) AND variation (e.g. standard deviation) or associated estimates of uncertainty (e.g. confidence intervals)
☐	☒	For null hypothesis testing, the test statistic (e.g. *F*, *t*, *r*) with confidence intervals, effect sizes, degrees of freedom and *P* value noted *Give P values as exact values whenever suitable.*
☒	☐	For Bayesian analysis, information on the choice of priors and Markov chain Monte Carlo settings
☒	☐	For hierarchical and complex designs, identification of the appropriate level for tests and full reporting of outcomes
☒	☐	Estimates of effect sizes (e.g. Cohen's *d*, Pearson's *r*), indicating how they were calculated

Our web collection on statistics for biologists contains articles on many of the points above.

Software and code

Policy information about availability of computer code

Data collection	Flow cytometry acquisition: BD FACSDiva™ version 6.1.1, 8.0.2 and 1.4, Cytek SpectroFlo version 2.2.0 Sorting: BD FACS™ version 1.2.0.142 Confocal Imaging: OLYMPUS™ FV31S-SW v2.3.2.169 Quantitative RT-PCR QuantStudio 7: QuantStudio Realtime PCR Software v1.3 Agilent TapeStation System Software Revision 4.1
Data analysis	Flow cytometry analysis: FlowJo version 10.7.1., OMIQ (v2020) Imaging analysis: FIJI imaging processing package (v2.0.0-rc-69/1.52i), CellProfiler (v4.0.3), Histocat (v1.76) GraphPad Prism 9.1.2 (v225) Bulk RNA-seq: Trimmomatic (v0.36), STAR (v2.7.1a), MultiQC (v1.7), R (v3.4.4), Rsubread (v1.28.1), DESeq2 (v1.28.1), pheatmap (v1.0.12), UpSetR (v1.4.0), Tidyverse (v1.3.0) Single cell RNA-seq: LAST (v1066), Salmon Alevin (v1.4.0), Seurat (v4.0.0), monocle3 (v1.0.0) Analysis of publicly available dataset: GSEA (v4.0.3), illuminaHumanv4.db R package (v1.26.0), Seurat (v3.2.0)

For manuscripts utilizing custom algorithms or software that are central to the research but not yet described in published literature, software must be made available to editors and reviewers. We strongly encourage code deposition in a community repository (e.g. GitHub). See the Nature Research guidelines for submitting code & software for further information.

Data

Policy information about availability of data

All manuscripts must include a data availability statement. This statement should provide the following information, where applicable:

- Accession codes, unique identifiers, or web links for publicly available datasets
- A list of figures that have associated raw data
- A description of any restrictions on data availability

The authors declare that the data supporting the findings of this study are available within the paper and its supplementary information files or are available from the authors upon reasonable requests.
For bulk RNA-seq and scRNA-seq data presented in figure 1, 2 and Extended data Figure 2: Raw RNA-seq data as FASTQ files have been deposited in NCBI SRA under bioproject PRJNA668222. All code and associated parameters are available at https://github.com/fronchese/Mayer_et_al_2020.
Figure 7 contains reanalysis of publicly available dataset: All code and associated parameters are available at https://doi.org/10.5281/zenodo.5534993.

Field-specific reporting

Please select the one below that is the best fit for your research. If you are not sure, read the appropriate sections before making your selection.

☒ Life sciences ☐ Behavioural & social sciences ☐ Ecological, evolutionary & environmental sciences

For a reference copy of the document with all sections, see nature.com/documents/nr-reporting-summary-flat.pdf

Life sciences study design

All studies must disclose on these points even when the disclosure is negative.

Sample size	Group sizes were chosen on the basis of previous experiments using the same methods and were found sufficient to reveal statistically significant differences (as determined using Prism software packages) and biologically relevant differences in the samples of interest.
Data exclusions	Flow data samples were excluded from consideration if they failed quality checks such as including sufficient numbers of the cell population of interest and within the range expected for the sample being examined, if sample viability was below expected level for the material being examined, or if sample acquisition was irregular due to equipment operation. Fewer that 1% of samples were excluded.
Replication	All experiments were repeated at least twice and and gave comparable results each time.
Randomization	Mice were allocated to experimental groups based on box numbers and were sex and age matched within experiments
Blinding	Investigators were not blinded to group allocation during data collection as data collection was carried out using instruments such as flow cytometers and RNA sequencers that are not affected by investigator bias.

Reporting for specific materials, systems and methods

We require information from authors about some types of materials, experimental systems and methods used in many studies. Here, indicate whether each material, system or method listed is relevant to your study. If you are not sure if a list item applies to your research, read the appropriate section before selecting a response.

Materials & experimental systems

n/a	Involved in the study
☐	☒ Antibodies
☒	☐ Eukaryotic cell lines
☒	☐ Palaeontology and archaeology
☐	☒ Animals and other organisms
☒	☐ Human research participants
☒	☐ Clinical data
☒	☐ Dual use research of concern

Methods

n/a	Involved in the study
☒	☐ ChIP-seq
☐	☒ Flow cytometry
☒	☐ MRI-based neuroimaging

Antibodies

Antibodies used	The following commercial antibodies were used, listed here by supplier/application. The following information is included in order: Specificity (Clone name): Catalog number (lot number if known), "Validation information provided by the supplier". [BioLegend] anti-CD103 (2E7): 121406 (B234254), “Flow cytometric analysis on mouse splenocytes”.

anti-CD11b (M1/70): 101235 (B298474), “Flow cytometric analysis of C57BL/6 mouse bone marrow cells”
anti-CD11c (N418): 117314 (unknown) "Flow cytometric analysis of C57BL/6 mouse splenocytes"
anti-CD124/IL-4Ra (I015F8), 144804 “Flow cytometric analysis on mouse splenocytes”.
anti-CD3 (145-2C11): 100320 (B268542), “Flow cytometric analysis of C57BL/6 mouse splenocytes”.
anti-CD326/EpCAM (G8.8): 118212 (B264359), “Flow cytometric analysis of mouse thymic epithelial stromal cell line TE-71.”
anti-CD4 (RM4-5): 100536 (B269384) “Flow cytometric analysis of C57BL/6 mouse splenocytes”.
anti-CD44 (IM7): 103012 (B264059), “Flow cytometric analysis on mouse splenocytes”.
anti-CD45R/B220 (RA3-6B2): 103226 (B258495), “Flow cytometric analysis on mouse splenocytes”.
anti-CD86 (GL1): 105018 (B234230), “Flow cytometric analysis on mouse splenocytes”.
anti-IA/IE (M5/114.15.2): 107622 (B264454); 107620 (B252427), “Flow cytometric analysis of C57BL/6 mouse splenocytes”.
anti-Ly6A/E (D7): 108138 (B240984), “Flow cytometric analysis on mouse splenocytes”.
anti-NK1.1 (PK136): 108703 (B298572), “Flow cytometric analysis on mouse splenocytes”.
anti-XCR1 (ZET): 148216 (unknown), “Flow cytometric analysis of C57BL/6 mouse splenocytes”.

[BD Biosciences]
Anti-CD117/c-kit (2B8): 562609 (5572837), “Multicolor flow cytometric analysis of CD117 expression on mouse bone marrow cells”.
anti-CD11c (HL3): 563735 (8043980), “Flow cytometric analysis of CD11c expression on mouse dendritic cells”.
anti-CD124/IL-4Ra (mIL4R-M1): 552508 (4827611), “Flow cytometric analysis of CD124 expression on mouse lymphocytes”.
anti-CD135/Flt3L (A2F10.1): 562537 (unknown), "Multicolor flow cytometric analysis of CD135 expression on C57BL/6 bone marrow cells".
anti-CD172a/Sirpa (P84): 560316 (4039483), “Flow cytometric analysis of CD172a expression on mouse bone marrow”.
anti-CD19 (6D5): 563557 (4493821), “Two-color flow cytometric analysis of CD19 expression on mouse splenocytes”.
anti-CD200R3 (Ba13): 567291 (4928374), “Two-color flow cytometric analysis of CD200R3 expression on mouse bone marrow cells”.
anti-CD24 (30-F1): 752760 (3392836), “Flow cytometric analysis of CD24 expression on mouse splenocytes”.
anti-CD25 (3C7) : 558643 (558272), “Flow cytometric analysis of CD25 expression on mouse splenocytes”.
anti-CD26 (H194-112): 559652 (6434811), “Two-color flow cytometric analysis of CD26 expression on mouse thymocytes”.
anti-CD278/ICOS (7E.17G9): 563469 (5732745), “Two-color flow cytometric analysis of ICOS (CD278) expression on activated mouse lymphocytes”.
anti-CD278/ICOS (C398.4A): 565883 (8403821), “Multi flow cytometric analysis of ICOS (CD278) expression on mouse thymocytes”.
anti-CD317 (927): 566431 (6620125), “Two-color flow cytometric analysis of CD317 expression on mouse splenocytes”.
anti-CD326/EpCAM (G8.8): 563134 (8072848, 9094621), “Flow cytometric analysis of BALB/c mouse thymocytes and splenic leukocytes”.
anti-CD45 (30-F11): 564279 (5843921), “Flow cytometric analysis of CD45 expression on mouse splenocytes”.
anti-CD45.1 (A20): 562452 (3048572), “Flow cytometric analysis of CD45.1 expression on mouse splenocytes”.
anti-CD45.2 (104): 561874 (3485711), “Flow cytometric analysis of CD45.2 expression on mouse splenocytes”.
anti-CD45R/B220 (RA3-6B2): 563793 (8269770), 553093 (3354876), “Flow cytometric analysis of CD45R expression on mouse splenocytes”.
anti-CD49b (DX5): 561066 (4884373), “Flow cytometric analysis of CD49b expression on mouse splenocytes”.
anti-CD64 (X54-5/7.1): 558455 (3594283), “Flow cytometric analysis of CD64 expression on mouse bone marrow cells”.
anti-CD8 (53-6.7) 560182 (3308752), 563332 (7214673), 558106 (9346019) “Two-color flow cytometric analysis of CD8a expression on mouse splenocytes”.
anti-CD90.2 (30-H12): 740334 (886241), “Flow cytometric analysis of CD90.2 expression on BALB/C mouse thymocytes”.
anti-FcεRIα (MAR-1): 566994 (8776354), “Flow cytometric analysis of FcεR1α expression on MC/9 cells”.
anti-GATA3 (L50-823): 560068, (7216782), “Comparison of GATA3 expression in human T and B cell lines”.
anti-IFN-γ (XMG1.2): 554411 (8099787, 9085768, 9197282), 566097 (6043664), “Flow cytometric analysis of stimulated (SEB) CD8+ and CD8- BALB/c spleen cells”.
anti-IL-4 (11B11): 554435 (9022663), 554436 (75631), “Flow cytometric analysis of BALB/c spleen cells stimulated with SEB for 72h and restimulated for 5h with anti-CD3 and anti-CD28 in the presence of monensin. Co-stained with anti-mouse CD4 FITC”.
anti-KLRG1 (2F1): 565393 (unknown) “Two-color flow cytometric analysis on mouse splenocytes”.
anti-Ly6C (AL-21): 563011 (7153555), “Flow cytometric analysis of Ly6C expression on mouse splenic leukocytes.”
anti-Ly6C/Ly6G (RB6-8C5): 553124 (8482921), “Flow cytometric analysis of Ly6C/Ly6G expression on mouse peripheral blood leukocytes”.
anti-RORγt (Q31-378): 562894 (8151861), “Multicolor flow cytometric analysis of RORγt expression in mouse thymocytes”.
anti-TCRγδ (GL3): 561996 (8298273), “Two-color analysis of the expression of TCR gamma delta on peripheral T Lymphocytes”.

[ThermoFisher Scientific]
Anti-CD11b (M1/70): 12-0112-82 (4712843), “Staining of mouse bone marrow cells with 0.06 µg of Anti-Mouse CD11b PE”.
anti-CD11c (N418): 17-0114-82 (2813421), “Staining of C57BL/6 splenocytes with Anti-Human/Mouse CD45R (B220) PE and 0.125 µg of Anti-Mouse CD11c APC (right)”.
anti-CD127/IL-7Ra (A7R34): 25-1271-82 (2755673), “Staining of BALB/c splenocytes with Anti-Mouse CD3e FITC and 1.0 µg of Anti-Mouse CD127 PE-Cyanine7.
anti-CD127a/Sirpa (P84): 13-1721-82 (4736463), “Staining of C57Bl/6 bone marrow cells with Anti-Mouse CD11b FITC and 0.125 µg of Anti-Mouse CD172a (SIRP alpha) Biotin followed by Streptavidin PE”.
anti-CD19 (ID3): 13-0193-82 (1924620), “Staining of C57BL/6 splenocytes with Anti-Human/Mouse CD45R (B220) APC and 0.125 µg of Anti-Mouse CD19 Biotin followed by Streptavidin PE”.
anti-CD206 (MR6F3): 17-2061-82 (4757239), “Mouse resident peritoneal exudate cells were surface stained with Anti-Mouse F4/80 Antigen eFluor® 450 followed by fixation and permeabilization with the Intracellular Fixation & Permeabilization Buffer Set. Cells were then intracellularly stained with 0.125 µg of Anti-Mouse CD206 (MMR) APC.
anti-CD123a/IL-13Ra1 (13MOKA): 12-2130-80 (2245987), “Splenocytes were cultured and stimulated with Anti-Mouse CD3 and Anti-Mouse CD28 for 3 days or harvested fresh on day 3 and then surface-stained with 0.25 µg of Anti-Mouse CD213a1 (IL-13Ra1) PE”.
anti-CD25 (PC6-1.5): 53-0251-82 (3957674), “Staining of BALB/c splenocytes with Anti-Mouse CD4 PE and Anti-Mouse CD25 Alexa Fluor® 488”.
anti-CD273/PD-L2 (TY25): 12-5986-82 (4736545), “Staining of mouse B7-DC-transfected cells with 0.06 µg of Anti-Mouse CD273 (B7-DC) PE”.
anti-CD3 (145-2C11): 25-0031-82 (2938236), “Staining of C57BL/6 splenocytes with Anti-Human/Mouse CD45R (B220) PE and 0.5 µg of Anti-Mouse CD3e PE-Cyanine7”.

anti-CD45R/B220 (RA3-6B2): 17-0452-82 (5634328), “Staining of C57BL/6 splenocytes with Anti-Mouse CD3 PerCP-eFluor® 710 and 0.125 µg of Anti-Human/Mouse CD45R (B220) APC”.
anti-FoxP3 (FJK-16s): 48-5773-82 (2735927), “Surface staining of C57BL/6 splenocytes with Anti-Mouse CD4 FITC followed by fixation and permeabilization with the Foxp3 Staining Buffers and intracellular staining with 0.03 µg of Anti-Mouse/Rat Foxp3 eFluor® 450”.
anti-GATA3 (TWAJ): 50-9966-42 (3113421), “Intracellular staining of BALB/c thymocytes with Anti-Mouse CD4 PE, Anti-Mouse CD8a FITC and Anti-Human/Mouse Gata-3 eFluor® 660 using the Foxp3 Staining Buffers”.
anti-IA/IE (M5/114.15.2): 56-5321-82 (3223384), “Staining of C57BL/6 splenocytes with Anti-Mouse CD3e FITC and 0.03 µg of Anti-Mouse MHC Class II (I-A/I-E) Alexa Fluor® 700”.
anti-IL-13 (eBio13A): 50-7133-82 (4492841), “BALB/c splenocytes were polarized under Th2 conditions for 3 days and then restimulated with Cell Stimulation Cocktail (plus protein transport inhibitors) for 5 hours. Following restimulation, cells were fixed and permeabilized and then intracellularly stained with Anti-Mouse CD4 FITC and 0.125 µg of Anti-Mouse IL-13 eFluor® 660”.
anti-IL-17A (eBio17B7): 25-7177-82 (4300417, 2093758), “Flow cytometric analysis of 10-day Th17-polarized mouse splenocytes and stimulated with Cell Stimulation Cocktail”.
anti-IL33R (RMST2-33): 12-9333-82 (4457564), “Staining of mouse bone marrow-derived mast cells with Anti-Mouse Fc epsilon Receptor I alpha (FceR1) FITC and 0.25 µg of Anti-Mouse ST2 (IL-33R) PE”.
anti-Ly6C/Ly6G (RB6-8C5): 13-5931-82 (4657212), “Staining of mouse bone marrow”.
anti-Ly6G (1A8): 48-9668-82 (2453446), “Staining of C57Bl/6 bone marrow cells with Anti-Mouse Ly-6C APC and Anti-Mouse Ly-6G (Gr-1) eFluor® 450”.
anti-NK1.1 (PK136): 11-5941-82 (4827376), “Staining of C57Bl/6 splenocytes with Anti-Mouse CD49b (Integrin alpha 2) eFluor® 450 and 0.25 µg of Anti-Mouse NK1-1 FITC”.
anti-pSTAT6(Tyr641) (46H1L12): 700247 "Western blot analysis of Phospho-STAT6 pTyr641 in Ramos lysate untreated (lane 1) or treated with IL-4 (lane 2) using a Phospho-STAT6 pTyr641 recombinant rabbit monoclonal antibody (Product # 700247) at a dilution of 2 µg/mL"
anti-Siglec H (eBio440c): 11-0333-82 (unknown), "Staining of SJL splenocytes with Anti-B220-PE, Anti-Mouse CD317-APC and 0.125 µg of Anti-Mouse Siglec H FITC"
anti-TCRβ (H57-597), 25-5961-82 (4392833), “Staining of C57Bl/6 splenocytes with Anti-Mouse CD4 eFluor® 450 and 0.06 µg of Anti-Mouse TCR beta PE-Cyanine7”.

[Tetramers]
5-OP-RU-loaded MR1 tetramer conjugated to BV421 was kindly provided by Dr. Olivier Gasser. Tetramers were generated at the NIH tetramer core facility and validated in the following publications (Pubmed ID: 29507084,30196233,29576482)..

[BioXCell]
InVivo anti-Thy-1: M5/49.4.1 (759254A2B), validated by previous studies listed at https://bxcell.com/product/m-thy-1/.

Validation

For commercially available antibodies, validation was performed by the manufacturer and their statements are cited in the box above for each antibody. In-house validation on appropriate target cells confirmed specificity.

Animals and other organisms

Policy information about studies involving animals; ARRIVE guidelines recommended for reporting animal research

Laboratory animals

The following mice were bred and housed under specific pathogen free (SPF) conditions, 21±3°C, 50±10% humidity, 12h/12h light/dark cycle at the Malaghan Institute of Medical Research, Wellington, New Zealand. All mice were between 6 and 14 weeks of age and were age and sex matched within experiments.

C57BL/6J (000664), BALB/cByJ (001026), B6-SJ ptprca (002014), Itgax-cre (008068), Irf4-flox (009380), STAT6-KO (005977), zDC-Cre (028538) and Il12b-YFP (006412) mice were originally obtained from the Jackson Laboratory (Bar Harbor, ME).

4C13R reporters (Tg(Il4-AmCyan,Il13-DsRed*)1Wep (Roediger et al., 2013) IL-4-KO (Il4tm1.1Wep) (Hu-Li et al., 2001) and TSLPR-KO (Crlf2tm1Wjl) (Al-Shami et al., 2004) mice were from breeding pairs kindly provided by the late Dr William Paul, NIAID, NIH, Bethesda USA.

IL4Ra-KO (Il4ra-tm1Fbb) (Mohrs et al., 1999) and IL-4Rα-flox (Il4ratm2Fbb) (Herbert et al., 2004) were from breeding pairs kindly provided by Dr Frank Brombacher, University of Capetown, South Africa.

MHCII-KO (H2-Aatm1Blt) (Kontgen et al., 1993) were bred from pairs originally provided by the late Dr Horst Bluethmann, Hoffman-La Roche Ltd, Basel, Switzerland. ST2-KO breeding pairs (Il1rl1tm1Aki) were from Dr Laura Mackay, University of Melbourne, Australia. Itgax-cre+/- Irf4fl/fl or fl/- and Irf4fl/fl or fl/- (IRF4WT) mice were generated by crossing Itgax-cre to Irf4fl for two generations. zBTB46-cre+/- Il4rfl/- and Il4rfl/- mice were generated by crossing Zbtb-cre females to Irf4fl for two generations.

IL-13-KO mice were generated by the Australian Phenomics Network and Monash Genome Modification Platform, Melbourne, Australia. CAS9 enzyme, guide RNA (gRNA) 1 targeting intron 1 (5’ - AGAGUCUUGGAGCUGAAAGA -3’) and gRNA2 targeting intron 3 (5’- CUUAGAGCGUUACAAGUCC- 3’) of the murine Il13 gene were injected into C57BL/6 fertilized eggs to remove exon 2 and 3. Mice were screened for exon deletion by PCR using the primers P1 (5’-GAGGCTGGCATGGTGGTTTC-3’) and P2 (5’-TGGAGACCTGTGAAACGGCA-3’). Of two founder mice carrying exon 2-3 deletions, only one gave viable progeny carrying the mutation when crossed to C57BL/6. These heterozygous mice were mated to each other to generate IL-13-KO mice carrying a homozygous exon 2-3 deletion and maintained at the Malaghan Institute of Medical Research.

For experiments at the NIAID, NIH (ambient temperature 22± 3°C, humidity 50±20%, light/dark cycle 14/10h), C57BL/6Tac and BALB/c were obtained from Taconic Biosciences (Rensselaer, NY) while B6.SJL-Ptprca Pepcb/BoyJ, RAG1-KO on C57BL6/J background, and IL13Ra1-KO on BALB/c background were from the NIAID contract facility at Taconic Biosciences. Germ-free C57BL/6 mice were bred and maintained in the NIAID Microbiome Program gnotobiotic animal facility.

CD4-Cre and iCOS-T (Icostm1.1(Hbegf)Anjm CD4-Cre)(Oliphant et al., 2014) mice were kindly provided by Dr Andrew McKenzie,

University of Cambridge, UK and were bred and maintained under SPF conditions with 22±2°C, 55±10% humidity and 12h/12h light dark cycle at the University of Manchester, Manchester, UK.

For all experiments, female mice were used unless otherwise indicated in Figure legends.

Wild animals: This study did not involve wild animals

Field-collected samples: This study did not involve samples collected from the field.

Ethics oversight: For experiments performed in New Zealand, experimental protocols were approved by the Victoria University of Wellington Animal Ethics Committee. Experiments at the NIAID were approved by the NIAID Animal Care and Use Committee, and experiments at the University of Manchester were performed under license of the UK Home Office and under approved protocols at the University of Manchester. All experiments were performed according to Institutional guidelines.

Note that full information on the approval of the study protocol must also be provided in the manuscript.

Flow Cytometry

Plots

Confirm that:

☒ The axis labels state the marker and fluorochrome used (e.g. CD4-FITC).

☒ The axis scales are clearly visible. Include numbers along axes only for bottom left plot of group (a 'group' is an analysis of identical markers).

☒ All plots are contour plots with outliers or pseudocolor plots.

☒ A numerical value for number of cells or percentage (with statistics) is provided.

Methodology

Sample preparation: To prepare single cell suspensions for DC assessment, auricular or inguinal LNs draining the skin, mediastinal LNs draining the lung or mesenteric LNs specifically draining the small intestine were disrupted with 18G needles and digested in IMDM containing 100 µg/mL Liberase TL and 100 µg/mL DNase I (both Sigma-Aldrich) for 30 minutes at 37°C. Cells were collected, filtered through a 70 µm cell strainer, washed with FACS buffer (PBS supplemented with 2% FCS, 2 mM EDTA and 0.01% Sodium Azide (all Gibco)) and maintained at 4°C. For skin preparations, ears were collected and split into ventral and dorsal halves, cut into small pieces and digested in 2ml HBSS (Gibco) containing 2 mg/mL Collagenase IV (Sigma-Aldrich) and 100 µg/mL DNase I (Sigma-Aldrich) for 30 minutes at 37°C and 250 rpm in a shaking incubator. The suspension was collected, dissociated using a syringe and 18G needle, filtered through a 70 µm cell strainer, washed with FACS buffer and maintained at 4°C. Lungs were collected after perfusion, cut into small pieces and digested in 1 ml IMDM (Gibco) containing 500 µg/mL Liberase TL and 500 µg/mL DNase I (both Sigma-Aldrich) for 45 minutes at 37° C and 150 rpm in a shaking incubator. Cells were collected, filtered through a 70 µm cell strainer, washed with FACS buffer and maintained at 4°C. Small intestine preparations were performed as previously described 83. Small intestinal segments were excised, Peyer's patches were removed and the intestines were opened longitudinally. Segments were then washed in PBS, cut into 0.5 cm pieces, collected in cold HBSS and washed twice with HBSS containing 2 mM EDTA (both Gibco) for 15 minutes at 37° C and 200 rpm in a shaking incubator to dissociate the epithelium. Segments were then digested in RPMI (Gibco) containing 10% FCS (Gibco), 1 mg/ml Collagenase VIII and 50 µg/ml DNase I (both Sigma-Aldrich) for 15-20 minutes at 37°C and 200 rpm in a shaking incubator. The suspension was then filtered through a 100 µm and 40 µm cell strainer, washed with FACS buffer and maintained at 4°C.
Skin-dLN preparations for the assessment of T cell responses were generated by pressing the LNs through a 70 µm cell strainer to obtain single cell suspensions, washed with FACS buffer and maintained at 4°C. For the assessment of intracellular cytokines in T cells, LN single cell suspensions were incubated in tissue culture medium (TCM, consisting of IMDM supplemented with 5% fetal calf serum (FCS), 1% Penicillin-Streptomycin and 55 µM 2-Mercaptoethanol (all Gibco)) containing 50 ng/mL PMA (Sigma-Aldrich), 1 µg/mL ionomycin (Sigma-Aldrich) and 1 µL/mL GolgiStop (BD Pharmingen) for 5 hours before proceeding with surface and intracellular flow cytometry staining.

Instrument: All samples were collected on a LSRFortessa SORP™, LSRII SORP™, FACSymphony SORP™ flow cytometer (all from Becton Dickinson) using BD FACSDiva™ software, or an Aurora spectral cytometer (Cytek Biosciences).

Software: Flow cytometry acquisition: BD FACSDiva™ version 6.1.1, 8.0.2 and 1.4, Cytek SpectroFlo version 2.2.0
Sorting: BD FACSTM version 1.2.0.142

Cell population abundance: For cell sorting experiments, the purity of relevant populations was greater than 95% as determined by reanalysis of a sample of sorted cells

Gating strategy: The gating strategies used in this study are reported in Supplemental data.
All flow cytometry data presented in this paper passed quality control in FlowJo v10. Cells were pre-gated on singlets, using sequential SSC-A v FSC-W and SSC-A v SSC-W gates, and live cells, by gating out DAPI+ or Live/Dead fixable dye+ cells. Debris was excluded using an FSC-A v SSC-A gate.

CD4+ T cells were defined as CD3+ and/or TCRβ+, CD4+, CD8-. Total CD4+ T cells were assessed for expression of CD44, IFNγ, IL-4, IL-17A, Tbet, Gata-3 or RORγt.

Dendritic cells were defined as B220- and/or CD19-, Ly6C-, CD11c mid-high and MHCII+. Monocytes were defined as B220- CD11b+ Ly6Chi CD64+. In some experiments, TCRβ+ and Ly6G+ cells were also excluded prior to DC/monocyte gating. Migratory DC were defined as CD11c mid-high and MHCIIhigh. MigDC subsets were identified as follows: LC (CD326+ XCR1-), DC1 (XCR1+), CD11b-high DC2 (CD326- XCR1- CD11b+), CD11b-low DC2 (CD326- XCR1- CD11blow).

Fluorescence minus one (FMO) controls assisted in defining positive and negative populations. PBS-injected mice served as staining controls for identifying Ag+ cells.

☒ Tick this box to confirm that a figure exemplifying the gating strategy is provided in the Supplementary Information.

Terms and Conditions

Springer Nature journal content, brought to you courtesy of Springer Nature Customer Service Center GmbH (“Springer Nature”).
Springer Nature supports a reasonable amount of sharing of research papers by authors, subscribers and authorised users (“Users”), for small-scale personal, non-commercial use provided that all copyright, trade and service marks and other proprietary notices are maintained. By accessing, sharing, receiving or otherwise using the Springer Nature journal content you agree to these terms of use (“Terms”). For these purposes, Springer Nature considers academic use (by researchers and students) to be non-commercial.
These Terms are supplementary and will apply in addition to any applicable website terms and conditions, a relevant site licence or a personal subscription. These Terms will prevail over any conflict or ambiguity with regards to the relevant terms, a site licence or a personal subscription (to the extent of the conflict or ambiguity only). For Creative Commons-licensed articles, the terms of the Creative Commons license used will apply.
We collect and use personal data to provide access to the Springer Nature journal content. We may also use these personal data internally within ResearchGate and Springer Nature and as agreed share it, in an anonymised way, for purposes of tracking, analysis and reporting. We will not otherwise disclose your personal data outside the ResearchGate or the Springer Nature group of companies unless we have your permission as detailed in the Privacy Policy.
While Users may use the Springer Nature journal content for small scale, personal non-commercial use, it is important to note that Users may not:

1. use such content for the purpose of providing other users with access on a regular or large scale basis or as a means to circumvent access control;
2. use such content where to do so would be considered a criminal or statutory offence in any jurisdiction, or gives rise to civil liability, or is otherwise unlawful;
3. falsely or misleadingly imply or suggest endorsement, approval , sponsorship, or association unless explicitly agreed to by Springer Nature in writing;
4. use bots or other automated methods to access the content or redirect messages
5. override any security feature or exclusionary protocol; or
6. share the content in order to create substitute for Springer Nature products or services or a systematic database of Springer Nature journal content.

In line with the restriction against commercial use, Springer Nature does not permit the creation of a product or service that creates revenue, royalties, rent or income from our content or its inclusion as part of a paid for service or for other commercial gain. Springer Nature journal content cannot be used for inter-library loans and librarians may not upload Springer Nature journal content on a large scale into their, or any other, institutional repository.
These terms of use are reviewed regularly and may be amended at any time. Springer Nature is not obligated to publish any information or content on this website and may remove it or features or functionality at our sole discretion, at any time with or without notice. Springer Nature may revoke this licence to you at any time and remove access to any copies of the Springer Nature journal content which have been saved.
To the fullest extent permitted by law, Springer Nature makes no warranties, representations or guarantees to Users, either express or implied with respect to the Springer nature journal content and all parties disclaim and waive any implied warranties or warranties imposed by law, including merchantability or fitness for any particular purpose.
Please note that these rights do not automatically extend to content, data or other material published by Springer Nature that may be licensed from third parties.
If you would like to use or distribute our Springer Nature journal content to a wider audience or on a regular basis or in any other manner not expressly permitted by these Terms, please contact Springer Nature at

onlineservice@springernature.com